Density, molar volume and surface tension of liquid Al-Ti

J. J. Wessing[1*], J. Brillo[1]

[1] Institute of Materials Physics in Space, German Aerospace Center (DLR), 51170 Köln, Germany

[*]Corresponding author:
Johanna Wessing
Institute of Materials Physics in Space,
German Aerospace Center (DLR), 51170 Köln, Germany
Tel.: +49 2203 601 3757
Fax: +49 2203 601 61768
E-Mail: Johanna.Wessing@dlr.de

Abstract

Al-Ti based alloys are of enormous technical relevance due to their specific properties. For studies in atomic dynamics, surface physics and industrial processing the precise knowledge of the thermophysical properties of the liquid phase is crucial. In the present work, we systematically measure mass density, ρ [gcm^{-3}], and the surface tension, γ [Nm^{-1}], as functions of temperature, *T*, and compositions of binary Al-Ti melts. Electromagnetic levitation in combination with the optical dilatometry method is used for density measurements and the oscillating drop method for surface tension measurements. It is found that, for all compositions, density and surface tension increase linearly upon decreasing temperature in the liquid phase. Within the Al-Ti system we find the largest values for pure titanium and the smallest for pure aluminum, which amount to $\rho_{(L,Ti)}$ = 4.12±0.04 gcm^{-3} and $\gamma_{(L,Ti)}$ = 1.56 ±0.02 Nm^{-1} and $\rho_{(L,Al)}$ = 2.09±0.01 gcm^{-3} and $\gamma_{(L,Al)}$ = 0.87 ±0.06 Nm^{-1}, respectively. The data are analyzed concerning the temperature coefficients, ρ_T and γ_T, excess molar volume, V^E, excess surface tension, γ^E, and surface segregation of the surface active component, Al. The results are compared with thermodynamic models. Generally, it is found that Al-Ti is a highly nonideal system.

Keywords

Al-Ti-alloys, density, surface tension, electromagnetic levitation, Butler model, Chatain model

49 **Table with used symbols**

ρ	mass density (g/cm3)
ρ_L	mass density at liquidus (g/cm^3/K)
ρ_T	temperature coefficient of mass density (10^{-4}g/cm^3/K)
ρ_i	mass density of component *i* (g/cm^3)
γ	surface tension (N/m)
γ_L	surface tension at liquidus (N/m)
γ_T	temperature coefficient of surface tension(10^{-4} N/m/K)
γ_i	surface tension of component *i* (N/m)
T	temperature (K (°C))
T_L	liquidus temperature (K (°C))
$T_{L,Ti}$	liquidus temperature of Ti (K (°C))
$T_{L,Al}$	liquidus temperature of Al (K (°C))
V^E	excess molar volume (cm^3/mol)
V	molar volume (cm^3)
V_i	molar volume of component *i*
V^{ideal}	molar volume of an ideal solution (g/cm^3/mol)
γ^E	excess surface tension (N/m/mol)
γ^{ideal}	surface tension of an ideal solution (N/m/mol)
β	thermal volume expansion coefficient
i,j	chemical species (Al or Ti)
x^B_i	mole fraction of component *i* in the bulk (at.-%)
X^S_i	mole fraction of component *i* in the surface (at.-%)
M_i	molar mass of component *i* (g/mol)
${}^{\nu}V$	Redlich-Kister volume parameter of ν-th order (cm^3/mol)
${}^{\nu}C$	Redlich-Kister volume parameter of ν-th order (cm^3/mol) at 0 K
${}^{\nu}D$	linear temperature coefficient of Redlich-Kister volume parameter of ν-th order (10^{-4}cm^3/mol/K)
R	universal gas constant (8.314 kJ/K/mol)
A	molar surface area (m^2/mol)
A_i	partial molar surface area of pure liquid *i* (m^2/mol)
${}^{E}G$	excess free energy (J /mol)

${}^{E}G_i^{B}$	partial excess free energy of component *i* in the bulk (kJ/mol)
${}^{E}G_i^{S}$	partial excess free energy of component *i* in the surface (kJ/mol)
f	geometrical factor
N_{Av}	Avogadro constant ($6.023\ 10^{23}$ mol^{-1})
ξ	factor accounting for a reduced coordination number in the surface
k	number of surface layers in the Chatain model
n	index of surface layer in the Chatain model
$x^{(n)}_i$	mole fraction of component *i* in the *n*-th surface layer
z	coordination number
z_l	lateral coordination number
z_v	vertical coordination number
$\Phi_{i,j}$	single bond energy for a bond between atoms *i* and *j* (J/mol)
ω	regular solution constant (J/mol)
${}^{\nu}L$	Redlich-Kister coefficient of ν-th order for the free energy (J/mol)
${}^{\nu}u(T)$	Redlich-Kister coefficient of ν-th order for the surface tension (N/m/mol)
T_P	pyrometer signal (K)
$T_{L,P}$	pyrometer signal at liquidus (K)
Rd	droplet radius (m)
φ	azimuthal angle
a_l	*l*-th edge curve coefficient
P_l	*l*-th Legendre polynomial
l	index
V_P	droplet volume in pixel units (pixel^3)
${}^{drop}V$	real droplet volume (cm^3)
q	scaling factor (cm^3/pixel^3)
Ω	mean translational frequency (s^{-1})
ω_x	translational frequency in x-direction (s^{-1})
ω_y	translational frequency in y-direction (s^{-1})
ω_z	translational frequency in z-direction (s^{-1})
ω_m	surface oscillation frequency of mode *m* (s^{-1})
g	gravitational acceleration (N/m^2)
R_0	radius of the sample with spherical shape (m)
p^S_{O2}	partial pressure of oxygen in the vicinity of the surface (Pa)

K	equilibrium constant (J/mol)
p^{Ch}_{O2}	partial pressure of oxygen in the chamber (Pa)
D_O	diffusion constant of oxygen in the vapor (m^2/s)
D_{Ox}	diffusion constant of oxide in the vapor (m^2/s)

1. Introduction

1.1. Al-Ti

The increasing need for more sophisticated materials in various high-temperature applications can potentially be satisfied by using Ti-based intermetallics. Even at elevated temperatures, γ-Al-Ti alloys combine a low density with a high tensile strength. This makes them particularly interesting for applications in the automotive or aerospace industries. For instance, they can be used as turbine blades in aircraft engines or as fuselage materials.

In addition, (α+β)-TiAl may also be used in medical applications as bone implants, because of their bio-compatibility and corrosion resistance. They also exhibit comparatively low densities and, compared to conventional implants made of Co-Cr- or Fe-based alloys, a small Young modulus of approximately 110 GPa. Compared to the Young-modulus of bones of approximately 25 GPa this is still high so further optimization of the material is necessary.

Therefore, developing a profound understanding of the liquid phase is indispensable, as the vast majority of materials are directly produced from the melt by casting [1]. Among the properties relevant in this context, density and surface tension of the liquid phase are of pronounced importance.

Density is a fundamental material property. Its knowledge is crucial for casting processes and for determining surface tension from the measured raw data.

Surface tension plays a critical role for the castability of an alloy, and for the mould-filling capability. The latter is often problematic in Ti-based alloys. Both properties also reveal interesting academic science as they are strongly affected by processes taking place at the atomic scale.

Despite the technical importance of density and surface tension, data on these properties of Ti-based alloys are sparse. The main reason for this is the high chemical reactivity of liquid Ti

paired with a large solubility of oxygen. This renders its investigation with conventional techniques extremely difficult. Nevertheless, there are containerbased methods, that have been used to investigate thermophysical properties of pure Ti and binary and multicomponent Al-Ti alloys, including the pendant [2] and sessile drop method [3]. Common methods for the determination of density and surface tension are listed in Table 1. The sessile drop method is applied to calculate the surface tension of a sessile drop, using the equilibrium dependence between the forces of surface tension and gravity. Additionally, density can be obtained from the drop profile by assuming axis-symmetry. When dealing with extremely reactive systems, such as Al-Ti, the difficulty of that method lies in finding an adequate inert substrate material that shows negligible interactions with the sample [2]. In the case of the pendant drop similar theoretical approaches are applied on liquid droplets, which are squeezed through a capillary. The advantage of the pendant drop method is that the contact of the sample with the capillary stays relatively short compared to the substrate contact [3]. Literature data on Ti and industrially used multicomponent alloys, such as $Al_{46}Ti_{46}X_8$, X=Nb, Ta and $Al_6Ti_{90}V_4$, along with their density and surface tension data are published in Refs. [1,4-23].

Typically, the main purpose of these investigations is the creation and completing of materials databases. However, if a detailed understanding of the system is envisaged, one must, perform measurements in which the composition is systematically varied [24].

The binary system Al-Ti is a good starting point for such investigations. To understand multicomponent systems, their binary basis must firstly be understood. Surprisingly, even for the binary system Al-Ti, data exist only in exceptional cases, such as for $Al_{80}Ti_{20}$ [25].

Therefore, the goal of the present work is to deliver systematically measured density and surface tension data on binary liquid Al-Ti alloys. Using electromagnetic levitation avoids pollution of the materials due to reactions with the container walls. Thus, the negative effects of the high chemical reactivity of the material are minimized. However, the interactions with

residual gas components of the surrounding environment (gas or vacuum) can still not be excluded. In particular, the role of oxygen needs to be discussed.

Density and surface tension measurements using levitation methods have been performed by us in the past on Al-based systems and systems containing Ti, such as Cu-Ti [26, 27], Al-Ni [24,28,29], Al-Cu [30,31], Al-Cu-Ag [32,33], Al-Ag [32,33], Al-Fe [24,28,29], Al-Au [34,35], Al-Si [36,37] and Al-Cu-Si [38]. The formalisms used for the interpretation and discussion of the measured data are described in the following.

1.2 Density, molar volume, and thermal expansion

Within a limited temperature interval including the liquidus point, the density $\rho(T)$ of a liquid metal can be considered as a linear function of temperature, T:

$$\rho(T) = \rho_L + \rho_T (T - T_L) \quad (1)$$

In this Equation, ρ_L is the density at the liquidus temperature, T_L, and ρ_T is the constant temperature coefficient $\partial\rho/\partial T$. The volume expansion coefficient, $\beta = V^{-1}(\partial V/\partial T)$, with V, being the molar volume of the liquid, ρ_T can be expressed as [24]

$$\rho_T = -\beta \cdot \rho_L \quad (2)$$

For a binary solution of components i (i = Al, Ti), with respective mole fractions x^B_i and molar masses M_i, the molar volume of the solution, $V=\rho^{-1}\sum x^B_i M_i$, is generally represented by [24]:

$$V = V^i + V^E, \quad (3)$$

with:

$$V^{ideal} = \sum_{i=Al}^{Ti} x_i^B \frac{M_i}{\rho_i} \quad (4)$$

Where ρ_i is the density of the pure substance i at temperature T. V^E is the excess volume and the index “B” of the mole fraction marks the amount of element i in the bulk.

For V^E=0, Eq. (3) reduces to a simple linear combination of the molar volumes of the pure liquid elements, $V_i=M_i/\rho_i$, and is designated as "ideal".

Generally, V^E depends on the temperature and the mole fraction. A simple expression of V^E is given by the following Redlich-Kister-type-Ansatz [24]:

$$V^{\mathrm{E}} = x_{\mathrm{Al}}^{\mathrm{B}} x_{\mathrm{Ti}}^{\mathrm{B}} \left(\sum_{v=0} {}^{v}V(T) (x_{\mathrm{Al}}^{\mathrm{B}} - x_{\mathrm{Ti}}^{\mathrm{B}})^{v} \right) \tag{5}$$

The parameters ${}^{v}V(T)$ represent the interaction between the elements Al and Ti in the alloy melt. As a first approximation, these parameters can be assumed to be linear functions of temperature with parameters ${}^{v}C = {}^{v}V(0\ \mathrm{K}\ (-273.15\ ^\circ\mathrm{C}))$ and $D^{v} = \partial {}^{v}V/\partial T$:

$${}^{v}V(T) = {}^{v}C + {}^{v}DT \tag{6}$$

1.3 Surface tension

As for the density, the surface tension $\gamma(T)$ can be expressed as a linear function of temperature, provided that the temperature interval considered is sufficiently small:

$$\boldsymbol{\gamma(T) = \gamma_{\mathrm{L}} + \gamma_{\mathrm{T}}(T - T_{\mathrm{L}})} \tag{7}$$

In this equation, γ_L is the surface tension at the liquidus temperature, T_L, and γ_T is the constant temperature coefficient. In order to quantitatively compare measured surface tension data with approximated model calculations by Butler [39], the liquid surface is considered as a monolayer of atoms. The layer is regarded as an individual thermodynamic phase being in equilibrium with the bulk. If x^S_i is the mole fraction of element *i* in the surface layer, γ can be calculated by solving the following set of equations known as the Butler equation [39]:

$$\begin{aligned} \gamma &= \gamma_{\mathrm{Al}} + \frac{RT}{A_{\mathrm{Al}}} \ln\left(\frac{x_{\mathrm{Al}}^{\mathrm{S}}}{x_{\mathrm{Al}}^{\mathrm{B}}}\right) + \frac{1}{A_{\mathrm{Al}}} \left({}^{\mathrm{E}}G_{\mathrm{Al}}^{\mathrm{S}}(\mathrm{T}, x_{\mathrm{Al}}^{\mathrm{S}}, x_{\mathrm{Ti}}^{\mathrm{S}}) - {}^{\mathrm{E}}G_{\mathrm{Al}}^{\mathrm{B}}(\mathrm{T}, x_{\mathrm{Al}}^{\mathrm{B}}, x_{\mathrm{Ti}}^{\mathrm{B}}) \right) \\ &= \gamma_{\mathrm{Ti}} + \frac{RT}{A_{\mathrm{Ti}}} \ln\left(\frac{x_{\mathrm{Ti}}^{\mathrm{S}}}{x_{\mathrm{Ti}}^{\mathrm{B}}}\right) + \frac{1}{A_{\mathrm{Ti}}} \left({}^{\mathrm{E}}G_{\mathrm{Al}}^{\mathrm{S}}(\mathrm{T}, x_{\mathrm{Al}}^{\mathrm{S}}, x_{\mathrm{Ti}}^{\mathrm{S}}) - {}^{\mathrm{E}}G_{\mathrm{Al}}^{\mathrm{B}}(\mathrm{T}, x_{\mathrm{Al}}^{\mathrm{B}}, x_{\mathrm{Ti}}^{\mathrm{B}}) \right) \end{aligned} \tag{8}$$

Here, R is the universal gas constant, and ${}^{\mathrm{E}}G_i^{\mathrm{B}}$ and ${}^{\mathrm{E}}G_i^{\mathrm{S}}$ denote the respective partial excess free energies of component *i* in the bulk and in the surface layer. A_i is the partial molar surface

area of pure liquid *i*, approximated by the following expression from the molar volumes of the pure elements V_i:

$$A_i = f V^{2/3} N_{Av}^{1/3} \quad (9)$$

In Eq. (9) N_{Av} is the Avogadro number, and *f* is a geometrical factor. The value of *f* depends on the structures assumed for the surface and the bulk. For liquids, the commonly used value of 1.09 has recently been regarded as too high [40]. A more reasonable value of $f = 1.0$ has been proposed by Kaptay [40] which is also used in the present work.

The main assumption of the Butler model is the approximation of the surface excess free energy ${}^{E}G^{S}_{i}(T, {}^{S}x_i)$ by ${}^{E}G^{S}_{i}(T, {}^{S}x_i)=\xi \cdot {}^{E}G^{B}_{i}(T, {}^{S}x_i)$, where the factor ξ accounts for the reduced coordination of atoms in the surface layer. It can be approached as the ratio of the respective coordination numbers of atoms in the surface and the bulk. A constant value of 0.75 was initially suggested by Tanaka and Iida [41] as default approximation for liquids with unknown structure. Later, they adjusted this value to 0.83 [42]. In this study, however, we use 0.75 in order to comply with the Chatain model that is also applied. Solving Eq. (9) yields the surface tension of the alloy and the concentration in the surface layer, x^{S}_{i}.

The Butler model may be criticized for its restriction to consider the surface as a phase of a single monolayer, neglecting concentration gradients perpendicular to the surface. On the other hand, as shown recently, [43], this phase does not necessarily need to be a mono-layer, as originally stated by Butler.

A different approach is followed by the Chatain model [44, 45] taking into account a concentration gradient as multiple layers, $n=1 \ldots k$, with different compositions, $x^{(n)}_{i}$, in each layer, *n*. The atoms of the liquid are assumed to reside on cubic lattice sites with a coordination number, $z=12$, in the bulk, and a lateral coordination number, $z_l=6$. The number of neighboring atoms in an adjacent atom layer is, thus, $z_v=3$. Interactions among atoms take place only with the nearest neighbors, where, $\Phi_{i,j}$ denotes a single bond energy for a bond

between atoms*i* and *j*. With this parameter the regular solution constant, ω, can be defined in Ref. [43] as $\omega = \Phi_{Al,Ti} - 0.5(\Phi_{Al,Al} + \Phi_{Ti,Ti})$. Assuming further that $\gamma_i = -z_v \Phi_{i,i}/2A$, the following expression is obtained for the surface free energy of a regular solution [43]:

$$\begin{aligned} A\gamma &= A\gamma_{Al}x_{Al}^{(1)} + A\gamma_{Ti}x_{Ti}^{(1)} \\ &- z_v\omega\left(x_{Ti}^{(1)} - 2x_{Ti}^{B}x_{Ti}^{(1)} - (x_{Ti}^{B})^2\right) - z_v\omega\sum_{n=1}^{k}(x_{Ti}^{(n)} - x_{Ti}^{B})(x_{Al}^{(n)} - x_{Al}^{B}) \\ &- z_l\omega\sum_{n=1}^{k}(x_{Ti}^{(n)} - x_{Ti}^{B})^2 \\ &+ RT\sum_{n=1}^{k}\left[x_{Ti}^{(n)}\ln\left(\frac{x_{Ti}^{(n)}}{x_{Ti}^{B}}\right) + x_{Al}^{(n)}\ln\left(\frac{x_{Al}^{(n)}}{x_{Al}^{B}}\right)\right] \end{aligned} \tag{10}$$

The parameters $\Phi_{i,i}$ and ω are related to the surface tension and the excess free energy, respectively, as follows:

$$\Phi_{i,i} = -A\gamma_i \tag{11}$$

And

$$\omega = -\frac{T^2}{z \cdot x_{Al}^{B}x_{Ti}^{B}}\frac{\partial}{\partial T}\left(\frac{^{E}G(T)}{T}\right) \tag{12}$$

The excess free energy, ^{E}G, used in Eqs. (8) and (10) is parametrized by a Redlich-Kister polynomial, as a function of concentration and temperature, with $^{\nu}L_{Al,Ti}(T)$ being temperature dependent interaction parameters:

$$^{E}G(T, x_{Al}, x_{Ti}) = x_{Al}x_{Ti}\sum_{\nu=0}{}^{\nu}L_{Al,Ti}(T)(x_{Al} - x_{Ti})^{\nu} \tag{13}$$

For a binary ideal solution, $^{E}G=0$, the following expressing is obtained for its surface tension γ^{ideal} [46]:

$$\gamma^{ideal}(T) = x_{Al}^{S}\gamma_{Al}(T) + x_{Ti}^{S}\gamma_{Ti}(T) \tag{14}$$

The deviation from the ideal surface tension, γ^{ideal}, is called excess surface tension, γ^{E} as:

$$\gamma = \gamma^{ideal} + \gamma^{E} \tag{15}$$

With this formalism, similar that one for the excess molar volume in section 1.2, γ^{E} may also be fitted analogously to a second order Redlich-Kister polynomial, with ${}^{\nu}u\,(T)$ being temperature-dependent interaction parameters:

$$\gamma^{\mathrm{E}} = x_{\mathrm{Al}}^{\mathrm{B}} x_{\mathrm{Ti}}^{\mathrm{B}} \left(\sum_{\nu=0}^{\mathrm{N}} {}^{\nu}u(T)\,(x_{\mathrm{Al}}^{\mathrm{B}} - x_{\mathrm{Ti}}^{\mathrm{B}})^{\nu} \right) \tag{16}$$

2. Experimental

Density and surface tension measurements are conducted in an electromagnetic levitation chamber described in detail in Ref. [47]. Typically, the alloy samples have diameters of 3 mm and masses of approximately 0.5 g. Inside the chamber the samples are positioned and melted by a spatially inhomogeneous electromagnetic field. This field is generated by a coil to which an alternating current of 100 A is applied with a frequency of approximately 250 kHz. Processing takes place under protective inert gas mixtures of He and Ar (both having a purity of 99.9999 %). Since, for electromagnetic levitation, positioning and heating are not generally decoupled, additional temperature control is provided by an adjustable cooling flow of inert gas, admitted to the samples via a nozzle.

The sample temperature, T, is measured using an infrared pyrometer directed to the specimen from the side. As the effective emissivity is not known in general, the pyrometer signal, T_{P}, needs to be recalibrated with respect to the known liquidus temperature, T_{L}, and the apparent liquidus temperature, $T_{\mathrm{L,P}}$. The apparent liquidus temperature is identified during the measurement by a kink in the pyrometer signal that appears, when the melting process is completed. The recalibration is accomplished using the following relation derived from Wien's law [48]:

$$\frac{1}{T} - \frac{1}{T_{\mathrm{P}}} = \frac{1}{T_{\mathrm{L}}} - \frac{1}{T_{\mathrm{L,P}}} \tag{17}$$

For metallic liquids, Eq. (17) gives a good approximation for the temperature, provided that the sample emissivity at the operating wavelength remains constant over the investigated

temperature interval [49]. For the pure elements and alloys, values of T_L are are shown in Tables 2, 3, 4 and 5 and taken from Ref. [50], using the CALPHAD approach to evaluate thermodynamic data. We have chosen the data as the used model is taking into account recent experimental data and is in close agreement with these data [50]. The phase diagram of the binary system of Al-Ti is shown in Fig. 1, respectively.

The preparation of the specific samples is performed by arc-melting the corresponding amounts of Al (99.999 %) and Ti (99.99 %). An ultrasound bath in propanol is used for cleaning and the removal of scales.

Finally, all samples are briefly heated up to a temperature of at least T_L+100 K**.** This produces further purification through evaporation of volatile Al-oxides.

The large difference in the melting temperatures of Al, 933 K (660 °C), and Ti, 1941 K (1668 °C), presents a challenge for the processing of the liquid alloys, due to the partially intense evaporation of Al. This may cause a shift in the sample mass and its composition. These effects may limit the accuracy of both density and surface tension data. Therefore, the mass loss of each sample is evaluated after each measurement and, in the event that it exceeds 0.1 % of the initial sample mass, the results are dismissed.

2.1 Density

The optical dilatometry method [30,47,51] is used to measure density and molar volume. This method employs lateral shadow images of the sample captured by a digital charge-coupled device (CCD) camera. The images are analyzed by an edge detection algorithm that determines the radius, *Rd*, with respect to the drop center and the azimuthal angle φ. The obtained curve, $Rd(\varphi)$, is averaged over 1000 frames in order to eliminate the influence of surface oscillations, and is then fitted by Legendre polynomials of order ≤ 6, where the brackets <..> denote averaging:

$$\langle Rd(\varphi)\rangle = \sum_{l=0}^{6} a_l P_l(\cos(\varphi)) \quad (18)$$

In Eq. (18), P_i is the *l*-th Legendre polynomial, and a_l are coefficients determined by the fit. The volume is calculated as following, assuming axial symmetry [30] of the droplet in mechanical equilibrium:

$$V_P = \frac{2}{3}\pi \int_0^{\pi} \langle Rd(\varphi)\rangle^3 \sin(\varphi) d\varphi \quad (19)$$

Here, V_P denotes the volume in pixel units. The real droplet volume, ${}^{drop}V$, is related to the pixel volume, V_P, by a scaling factor, q with ${}^{drop}V = qV_P$. q is obtained by a calibration procedure described in Ref. [28q]. Finally, the density is calculated with respect to the sample mass, *M*, by $\rho = M/{}^{drop}V$. Following this procedure the obtained results are accurate within $\Delta\rho/\rho \leq \pm 1.0$ % [24,30].

2.2 Surface tension

The oscillating droplet method [47] is applied to determine surface tension. In this method spontaneously self-excited surface oscillations are observed by means of a digital complementary metal oxide semiconductor (CMOS)-camera directed at the sample from above. The camera has a pixel resolution of 400x400, and operates at a frequency of 400 Hz. A series of $2^n = 4196$ frames is recorded for each investigated temperature and, these are then analyzed afterwards with dedicated software that determines the frequency spectra of the sample radii, *R*, from the image sequences. Under terrestrial conditions i.e. in the case of a non-spherical and slightly rotating droplet the spectrum consists of five distinguished peaks, at frequencies ω_m, corresponding to the surface oscillation modes, with *m* being a quantum number from, in this case, -2 to +2 [47]. Additionally, the three translational frequencies ω_X, ω_Y, ω_Z, can be identified from the motion of the droplets' centers of gravity, and thus the mean quadratic translational frequency can be calculated as:

$$\Omega^2 = \frac{1}{3}(\omega_X{}^2 + \omega_Y{}^2 + \omega_Z{}^2) \quad (20)$$

From the five surface oscillations and three translational frequencies, the surface tension, γ, is determined using the sum formula of Cummings and Blackburn [51], where g denotes the gravitational acceleration and R_0 the radius of the sample, which is assumed to be spherical:

$$\gamma = \frac{3M}{160\pi}\sum_{m=-2}^{+2} {\omega_{\mathrm{m}}}^2 - 1.9\Omega^2 - 0.3\left(\frac{g}{R_0}\right)^2 \Omega^{-2} \quad (21)$$

This procedure allows the precise determination of the surface tension within a margin of $\Delta\gamma/\gamma \leq 5.0$ % [24]

3. Results

3.1 Density

Measured density data are plotted in Fig. 2, versus temperature for liquid samples with Al-mole fractions x_{Al}, ranging from 0 to 100 at.-%. Each measurement is carried out over a broad temperature range, of 150-500 K, including up to 200 K undercooling below the corresponding liquidus temperature. Generally, the temperature range is limited by the nucleation of the solid phase at low temperatures and by mass loss due to evaporation at sufficiently large temperatures.

For all compositions, the density, ρ, changes linearly with temperature and with a negative slope, indicating a positive thermal volume expansion coefficient. Moreover, the density changes gradually with $x_{\mathrm{Al}}^{\mathrm{B}}$. Pure Al exhibits the lowest density, and Ti the largest. The density values of the alloys lie within these two extremes.

The experimentally obtained values of $\rho(T)$ can be fitted by Eq. (1) with the fits shown in Fig. 2 by the solid lines. The obtained values of ρ_{L} and ρ_{T}, as well as the volume expansion coefficient, β, calculated from this data via Eq. (2), are listed along with in Tables 2, 3, and 6 along with the corresponding liquidus temperatures. Accordingly, Table 2 contains the results for the pure elements and Table 3 contains the results for the alloys.

In the case of pure Al, the agreement among the values of ρ_L is around a mean value of 2.30 gcm^{-3}, within ±0.02 gcm^{-3}, corresponding to a relative uncertainty of ±0.09 %. The values of ρ_T are distributed around a mean of $-2.18 \cdot 10^{-4}$ $gcm^{-3}K^{-1}$, within $\pm 0.32 \cdot 10^{-4}$ $gcm^{-3}K^{-1}$, corresponding to ±15 %. In the case of Ti, the average of the individual values of ρ_L amounts to 4.12 (±0.04) gcm^{-3}, corresponding to a relative deviation of 1 %. The temperature coefficient of pure Ti scatters around $-2.85(\pm 1.24) \cdot 10^{-4}$ $gcm^{-3}K^{-1}$ and, hence, within a relative margin of 35 %. Generally, it is observed for our measurements that the deviations in ρ_T are in the range of up to 50 %, as its precise determination is sensitive to the accuracy of the data points, determined at the margins of the temperature intervals. These are, however, the points that are most exposed to the impact of potential sources of error, such as evaporation at high temperatures, or possible oxide formation, for example at low temperatures.

Table 6 contains data for ρ_L and ρ_T, and their mean values selected from literature [4, 35-45,52]. In the case of pure Ti mean values of 4.17 (±0.07) gcm^{-3}, for ρ_L and $-4.18 \cdot 10^{-4}$ $(\pm 3.02 \cdot 10^{-4})$ $gcm^{-3}K^{-1}$, for ρ_T can be found. Thus, the data presented in the present work is in good agreement with the literature and lies within the error for the mean value of pure Ti. Accordingly, for pure Al the mean value of the temperature coefficient of the present work, $-2.85(\pm 1.24) \cdot 10^{-4}$ $gcm^{-3}K^{-1}$, agrees well with the mean temperature coefficient value of the selected literature data of $-2.91(\pm 0.5) \cdot 10^{-4}$ $gcm^{-3}K^{-1}$. However, for the mean value of ρ_L for pure Al, the value of the present work, 2.30(±0.02) gcm^{-3}, is lower and lies beyond the errors bars of the mean value, 2.36 (±0.03) gcm^{-3}, given by literature, see Tabs. 2 and 6. The reason is unclear.

In Table 3 the values of ρ_L change gradually with increasing x_{Al}^B. Except for $Al_{40}Ti_{60}$, $Al_{60}Ti_{40}$ and $Al_{90}Ti_{10}$, all compositions are measured more than once, and, in these cases, the observed scatter in ρ_L and ρ_T is in the same order of magnitude as for the pure elements. For ρ_T this margin is about 40 %, which corresponds to the magnitude of the variation among the

different values of ρ_T over all compositions. Hence, it is justified to claim that with respect to the experimental accuracy of the data, ρ_T is basically constant with a mean value of -3.83 ($\pm$1.6)·10^{-4} gcm^{-3}. The same holds for β, for which a mean value of 1.18 ($\pm$0.5)·10^{-4} K^{-1} is found over all compositions.

In addition to ρ_L, ρ_T and β, the Tables 6 and 7 also show the isothermal density calculated from Eq. (1) at T=1873 K (1600 °C). This temperature is chosen to be in the middle of the total range of temperatures covered by the experiments. As can be seen from the Tables, ρ(T=1873 K (1600 °C)) decreases monotonically from ρ_{Ti}=4.14 ($\pm$0.04) gcm^{-3} to ρ_{Al}=2.09 ($\pm$0.01) gcm^{-3} upon increasing x_{Al}^{B}.

In order to elucidate and understand how the density changes with composition, it is indicated not to discuss the mass density but rather the isothermal molar volume, V and its composition dependence. In contrast with mass density, the molar volume is an additive quantity. Moreover, effects originating from the packing and ordering of atoms could be obscured by the mass differences between the pure elements, Al and Ti, if only the mass density is considered.

For this reason, the molar volume at 1873 K (1600 K) is plotted in Fig. 3 versus x_{Al}^{B}. For some alloys this temperature lies outside the measured temperature range, due to the aforementioned temperature range boundaries. For these alloys, the density is extrapolated by Eq. (2). This is marked in Fig. 3 by hollow or semi-hollow symbols. The precise location of the phase boundaries is not crucial in this context, as the properties of the stable (or metastable) liquid are of primary interest.

As can be seen from Fig. 3, the molar volume, V, generally increases with an increasing mole fraction of respective mean values of the pure elements, x_{Al}^{B}, from 11.54 cm^{3}mol^{-1} to 12.92 cm^{3}mol^{-1}.

317 Starting on the left side in Fig. 3, there seems to the tendency that *V* slightly decreases for
318 $x_{\mathrm{Al}}^{\mathrm{B}}$< 40 at.-%. However, this tendency is beyond the scatter of the experimental data.
319 Therefore, *V* can be regarded as practically constant at ≈11.5 cm^3mol^{-1} for $x_{\mathrm{Al}}^{\mathrm{B}}$< 70 at.-%. For
320 $x_{\mathrm{Al}}^{\mathrm{B}} \geq$ 70 at.-%, however, *V* steeply increases with $x_{\mathrm{Al}}^{\mathrm{B}}$ until its final value is reached at
321 $x_{\mathrm{Al}}^{\mathrm{B}}$=100 at.-%.
322
323 3.2 *Surface tension*
324 Surface tension data of the liquid pure elements is plotted versus temperature in Fig. 4 for Al
325 and in Fig. 5 for Ti. In the case of Al, the data shown is published by us previously [24,33].
326 The experimentally obtained values of $\gamma(T)$ follow linear laws and hence, can be fitted by Eq.
327 (7).
328 In the case of pure Ti, the solid squares shown in Fig. 5 represent three individual
329 measurements which are combined to a single curve. For each of these measurements, the
330 obtained fit parameters γ_L and γ_T are shown in Table 4. From these, arithmetic averages are
331 formed which are shown in Tab. 4 as well, and additionally, in Tab 8. The mean of γ_L
332 amounts to 1.56(±0.02) Nm^{-1}. Its' uncertainty corresponds to a relative deviation of ±1.3%.
333 The temperature coefficient of pure Ti scatters around (-1.65(±0.95))·$10^{-4}Nm^{-1}K^{-1}$, and hence,
334 within a relative margin of ±58 %. Generally, it is observed that the deviations in γ_T are in the
335 range of up to 58 %, which is larger than the deviations in the surface tension, γ. This is for
336 essentially the same reasons as the increased scatter in ρ_T. For comparison, Fig. 5 and Tab. 8
337 also show surface tension data of liquid Ti, or their linear representations, as obtained in
338 literature. Excellent agreement is obviously obtained with the data published by Paradis [53]
339 who measured γ in electrostatic levitation.
340 Fig. 4 shows two sets of experimental surface tension data of liquid Al. The hollow circles
341 represent data that has been measured by Kolland [35] whereas no particular attention was

paid to the oxygen partial pressure. It has been concluded in Ref. [35] that this result corresponds to a case where the surface contains a significant amount of dissolved oxygen. Fitting Eq. (7) to this data yields γ_L=0.87 Nm^{-1} and γ_T=-1.46·$10^{-4}$$Nm^{-1}K^{-1}$. This is roughly 5 % larger than data reported by Molina [54] for an oxygen saturated liquid surface, see Fig. 4. The solid squares in Fig. 4 represent the measurement of Kobatake [37] where the oxygen partial pressure was controlled **(**10^{-1} Pa**)** using an oxygen sensing and control system (OSC). The obtained curve is in good agreement with the results of Molina who presented in his study [54] also surface tension data for an oxygen free Al surface. In Fig. 4, the results of Kobatake even overestimate the data of Molina slightly. Fitting Eq. (7) to the data of Kobatake [37] yields γ_L=0.98 Nm^{-1} and γ_T=-2.71·$10^{-4}$$Nm^{-1}K^{-1}$. For Al, the parameters γ_L and γ_T are listed in Table 4. Detailed discussions of the surface tension of liquid Al are further presented in refs. [35,37].

Figure 6 shows plots of γ versus temperature for the liquid alloy samples. For the sake of completeness and in order to be able to make visual comparisons, the figure also shows the data for pure Ti and representations of the data of pure Al taken from refs. [35,37].

The Al-mole fraction, x_{Al}^{B}, ranges from 0 to 100 at.-% in Fig. 6. Each measurement is carried out over a broad temperature range of 100-250 K, including up to 200 K undercooling below the corresponding liquidus temperature. Corresponding to the density, surface tension measurements are restricted by the same temperature range boundaries.

For all compositions it is found again that γ linearly declines with temperature. Moreover, γ changes gradually with x_{Al}^{B}, and exhibits an increase from the lowest values for pure Al, to the highest γ for pure Ti.

The individual fits of Eq. (7) are shown in Fig. 6 by the solid lines. The obtained values of γ_L and γ_T are listed in Tab. 5 for the alloy system, together with the corresponding liquidus temperatures T_L.

As shown in Tab. 5, the values of γ_L change gradually with increasing x_{Al}^B. For multiple data of the same alloys, the observed scatter for γ_L and γ_T ranges in the same order of magnitude as for the pure elements. In particular, for γ_T, the margin for all compositions is around 55 %**.** That agrees well with the magnitude of variation among the γ_T data of each compositions of 20-60 %. Hence, it is justified to claim that, with respect to the experimental accuracy of the data, γ_T is essentially constant, with a mean value of $(-2.51(\pm1.37))\cdot10^{-4}\mathrm{Nm^{-1}K^{-1}}$.

In addition, Tables 4 and 5 show the isothermal surface tension calculated from Eq. (7) at T=1950 K (1677 °C), chosen from the middle of the total range of temperatures covered by the experiments. As can be seen from the Tables, $\gamma(T$=1950 K (1677 °C)) decreases monotonically from γ_{Ti}=1.56(±0.02) $\mathrm{Nm^{-1}}$ to γ_{Al}=0.71(±0.01) $\mathrm{Nm^{-1}}$ upon increasing x_{Al}^B. In Fig. 7 the surface tension at T=1950 K (1677 °C) is plotted versus x_{Al}^B. Analogously to the density data, the extrapolated value for $\gamma(T$=1950 K (1677 °C)) partially outlies the measured temperature range for some alloys, which is negligible in the context. Starting on the left side in Fig. 7, $\gamma(T$=1950 K (1677 °C)) decreases with concentration for component x_{Al}^B < 20 at.-%. There appears to be the tendency that $\gamma(T$=1950 K (1677 °C)) does not decrease, and is approximately constant for 20 at.-%. $\leq x_{Al}^B \leq$ 30 at.-%. However, this tendency is beyond the scatter of the experimental data. For x_{Al}^B> 30 at.-%, $\gamma(T$=1950 K (1677 °C)) steeply decreases with x_{Al}^B, and exhibits a concave shape until its final value is reached at x_{Al}^B =100 at.-%.

4. Discussion

4.1. Density

In addition to the experimental data, the calculated ideal molar volumes, V^{ideal}, at T=1873 K (1600 °C), are plotted versus the bulk Al concentration in Fig. 3. Accordingly, the molar volumes of the pure components used for the calculation are assessed from the averaged density values at T=1950 K, with $\rho_{Al} = 2.09\ \mathrm{gcm^{-3}}$ and $\rho_{Ti} = 4.14\ \mathrm{gcm^{-3}}$. The deviation

between the measured molar volume, V, and the ideal molar volume, V^{ideal}, corresponds to the excess molar volume, V^E Eq. (4). In Fig. 3, $V(x_{Al}^B)$ is fitted by a Redlich-Kister polynomial of zeroth ($N = 0$) and first ($N = 1$) order. The fitted, temperature-dependent excess parameters, ${}^0V$and ${}^1V$, are listed in Tab. 7. Regarding V^{ideal} and V, the fits exhibit a negative deviation, and hence, the excess volume is negative. For a fitted excess molar volume with N=0 in Eq. (4), the molar volume shows a concave shape, with the maximum negative excess molar volume for an Al concentration, $x_{Al}^B \approx 20$ at.-% of around -0.37 $10^{-6}m^3mol^{-1}$. Starting from the left side for a fit with N=0 in Eq. (4), V slightly increases for x_{Al}^B < 16 at.-%, and shows a minor local maximum at x_{Al}^B = 16 at.-%. For 16 at.-% < x_{Al}^B< 67at.-%, V slightly decreases with a maximum negative excess molar volume, $V^E \approx$ -0.8 $10^{-6}m^3mol^{-1}$, for x_{Al}^B = 67at.-%. For $x_{Al}^B \geq$ 67 at.-%, V steeply increases with increasing Al concentration, until its final value is reached at x_{Al}^B=100 at.-%. In contrast to V^i, both fits are in good agreement with the data. Consequently, it can be said that, referring to the density and molar volume, Al-Ti is a highly nonideal system, showing significant negative excess volumes.

However, the fit of first order reproduces the data and its trend more accurately. Thus, we suggest, in the case of binary Al-Ti, two fit parameters, ${}^0V$ and ${}^1V$, are needed to describe the excess molar volume. This is in accordance with other binary Ti-containing systems, where two fit parameters are used to fit the data qualitatively and quantitatively well; for example, in the case of Cu-Ti [26, 27]. However, a positive excess volume has been found in the case of Cu-Ti. Negative excess molar volumes have been found in other Al-containing systems such as Al-Fe [28], Al-Ag [30], Al-Cu [20] and Al-Ni [28], hence, the results are in good agreement with literature data, for example, with the investigations by Peng et al. for the Al-Au system [34]. Density measurements and molecular dynamics (MD) simulations in that system suggest that the nonideal mixing behavior occurs due to the apparent decreasing atomic radii of the Al atoms. This leads to a shrunken close packing, especially of the Al-Al

pairs [34]. Taking this into account, similar processes in the Al-Ti system are likely, but further investigations, e.g. MD simulations, experiments with neutron or X-ray scattering are required to confirm this.

Fig. 8 shows plotted and fitted isothermal excess molar volumes, V^E, as a function of the Al concentration, x_{Al}^B, for different temperatures (T = 1473 K (1200 °C), 1673 K (1400 °C), and 1873 K (1600 °C)). Corresponding to its definition, the excess molar volume for the pure elements Al and Ti equals zero. For all temperatures, the values show a concave shape. Starting from the left side, V^E decreases until its maximum negative values of around $V^E \approx$ -0.80-1.05 $10^{-6} m^3 mol^{-1}$ for $x_{Al}^B \approx$ 60-70 at.-%. Accordingly, the maximum negative excess molar volumes decrease with increasing temperatures, while their values also shift to higher Al concentrations. This shift indicates, that a more efficient packing and interaction occur for lower temperatures, as pronounced atomic mobility and dynamics at higher temperatures suppress those interactions and entropy becomes dominant.

4.2 The role of oxygen

Due to high affinity of oxygen to both elements, Al and Ti, the impact of potentially existing traces of oxygen on the surface tension needs to be discussed.

In the case of pure liquid Al, the effect is demonstrated in Fig. 4. In the case of Kobatake's measurement, the oxygen partial pressure in the chamber p^{Ch}_{O2} was adjusted at roughly 10^{-1} Pa. This is far above the equilibrium partial pressure, 10^{-25} Pa, for Al_2O_3 formation [55]. However, it has been argued by Eustathopolous [56] that the evaporation of volatile Al_2O effectively lowers the oxygen partial pressure p^S_{O2} in the vicinity of the surface. This can be described by the following equation:

$$p^S_{O2} = \{(2D_O/D_{Ox}) p^{Ch}_{O2}/K\}^2 \approx (p^{Ch}_{O2}/K)^2 \quad (22)$$

where K is the equilibrium constant of the reaction and D_O and D_{Ox} indicate the diffusion coefficients of oxygen and the oxide in the vapor, respectively. In the case of pure Al, the

443 effective partial pressure of the sample, $p^{S}_{O2,}$ can be estimated as 10^{-26} Pa, which is well
444 below the equilibrium pressure and the surface tension measured by Kobatake for liquid Al
445 can be regarded as reliable.
446 In the case of pure Ti, the situation is more complicated. A detailed thermodynamic analysis
447 on oxygen in liquid Ti performed by Belyanchikov [57] shows that there are no volatile
448 oxides in this system. Ti can reduce liquid Al and consequently capture all oxygen from Al if,
449 as in the present work, liquid Al-Ti is investigated. Belyanchikov [57] furthermore showed
450 that Ti can practically not be reduced by any of the strongest deoxidizers known, i.e. Ba, Be,
451 Ca, Ce, Hf, La, Mg, Sr, Zr, and Fe. The oxygen content of one of the solidified Ti samples
452 was determined in a LECO analysis after the levitation run. It was found that its oxygen
453 concentration was approx. 0.15 %. This value agrees with the maximum solubility of oxygen
454 in liquid Ti predicted by Belyanchikov [57] under the assumption that Ti is in contact with an
455 oxide.
456 On the other hand, Paradis argued in his work that his surface tension data on pure and
457 oxygen-free liquid Ti should be correct, because pronounced evaporation of liquid Ti might
458 induce a self-purification process of the sample [53]. It is evident that both datasets of the
459 surface tension of liquid Ti, the one of Paradis and of the present work, belong to the highest
460 values obtained in Fig. 5. Most of the other data, including the one measured by Amore [27],
461 are lower. This fact indicates that oxygen, if dissolved in the liquid Ti samples, does not play
462 a significant role in the case of the present work.
463
464 *4.3 Surface tension*
465 A comparison of the experimental data and model calculations for the isothermal surface
466 tension, $\gamma(T$=1950 K (1677 °C)), is shown in Fig. 7. The data are fitted by a Redlich-Kister
467 type polynomial of first (N=1) order. The corresponding fit parameters, ${}^{0}u(T$=1950 K (1677
468 °C)) and ${}^{1}u(T$=1950 K(1677 °C)), for the excess surface tension of the measured data are

listed in Tab. 7. The fit is in good agreement with the data and lies within the error bars for all Al concentrations. Generally, the fit follows the curvature of the data, except for 10 at.-% < $x_{\mathrm{Al}}^{\mathrm{B}}$ <30 at.-%, where it does not reproduce the kink, and slightly overestimates the surface tension.

The model for an ideal solution, following Eq. (15), exhibits a concave shape, with its highest values for pure Ti and lowest values for pure Al. The model does not reproduce the data qualitatively, and underestimates the values for all alloys except for $Al_{90}Ti_{10}$. Hence, the model fails to describe the data correctly and Al-Ti does not show ideal solution behaviour, analogously to density, excess free energy and other Al- and Ti-based alloys.

A far better agreement is obtained for the calculations by the Butler model, Eq. (9) with the temperature dependent interaction parameters, ${}^{\mathrm{v}}L_{\mathrm{Al,Ti}}(T)$, listed in Tab. 7 and Chatain model [44,45] for subregular nonideal solutions. The surface tension and its concentration dependence are predicted qualitatively with both models, showing positive excess values, regarding the ideal solution. The Butler model shows a good agreement, in particular for 25 at.-% ≥ $x_{\mathrm{Al}}^{\mathrm{B}}$ ≥50 at.-%. In this interval the model follows the curvature of the data and lies within all error bars. Nevertheless, for 25 at.-% < $x_{\mathrm{Al}}^{\mathrm{B}}$ < 50 at.-% the Butler model underestimates the data by 5-16 % and does not reproduce the kink, shown by the data for those concentrations. On the other hand, the calculations of the Chatain model [44,45] reproduce the kink for an Al concentration around 25-50 at.-%, but overestimate $\gamma(T$=1950 K (1677 °C)) for 40 at.-% < $x_{\mathrm{Al}}^{\mathrm{B}}$ <70 at.-% by 5-12 %. Although the Chatain model lies within the error bars for Al concentrations greater than 70 at.-%, the model predicts a negative kink in this interval, while the data follows a minor a positive kink.

Overall, it is suggested that the Butler model for nonideal solutions reproduces the data most accurately in the Al-Ti system. Usually, the ideal solution fails to predict experimental data correctly, as for most systems, the excess free energy, ${}^{\mathrm{E}}G \neq 0$. For ideal solutions only the surface segregation of the surface active component is taken into account e.g. Al in the case of

Al-Ti but other inter-atomic effects are neglected. Surface segregation can be understood as a process of energy minimization, in order to minimize the energy of the system, G_{tot}, the component with the smaller surface tension becomes enriched in the surface layer. For alloys with ${}^{E}G > 0$, the surface segregation becomes enhanced, while for alloys with ${}^{E}G < 0$, the surface segregation of Al is suppressed, due to interatomic attractions. The latter is found for many Al-systems, such as Al-Cu, Al-Ni, Al-Fe and Al-Au, as reported by Brillo et al. [24], and leads to an increased surface tension, compared to the ideal system, as in the case of Al-Ti.

The suppressed Al surface segregation of the nonideal solution, in comparison with the ideal solution is also calculated with the Butler model [39] for a monolayer, and the Chatain model [44, 45] for multiple layers, displayed in Fig. 9. Here, the Al-content of the surface is plotted against the Al-content of the bulk. For all models a general Al segregation is evident in an enriched Al-content in the surface versus the bulk. Compared to the ideal solution, for $x_{\mathrm{Al}}^{\mathrm{B}} \leq$ 60 at.-% the concentration of the top layer is relatively depleted by Al, by up to 40 % for the Butler model and up to 60 % for the Chatain model. For Al concentrations higher than 60 at.-% for the Butler model, and 80 at.-% for the Chatain model, no further suppression of the segregation is predicted by the models.

As can be seen in Figs. 9 and 10, the Chatain model gives highly fluctuating values of Al enrichment and depletion for the uppermost layers. Fig. 10 shows the concentration, $x_{\mathrm{Al}}(n)$, of each layer plotted against the layer number, n, for $Al_{50}Au_{50}$, at T=1700 K (1427 °C), T=1950 K (1677 °C). While, with respect to the bulk, the first layer exhibits an enrichment of Al of around 25 %, the second layer shows a depletion of Al of around 10 %. This oscillating behaviour continues for both temperatures in the figure, until, in the layer, n=6, the bulk composition is reached. Such concentration oscillations are called chemical layering. In this mechanism the segregation of one component to the surface leads to an excess of the other component in the following layer. Due to the negative excess free energy, the other

component is then favored in the second layer. Chemical layering has been observed in several systems with negative excess free energy; for example in the cases of Al-Ni [29], Al-Cu [31] and Al-Au [35]. For T=1700 K (1427 °C), the chemical layering is slightly more pronounced than for T=1950 K (1677 °C), due to the minor atomic dynamics at low temperatures and, thus, enhanced interactions between atoms.

The values for the temperature coefficient, γ_T, experimentally obtained, and the values calculated by the Chatain and Butler model, are plotted in Fig. 11. As γ_T was assumed to be constant, with a mean value of -2.51(±1.37) 10^{-4}·$Nm^{-1}K^{-1}$, the Butler model, with a mean value of -2.14(±0.89) 10^{-4}·$Nm^{-1}K^{-1}$, is, regarding the temperature coefficient, also in better agreement with the data than the Chatain model with a mean value of -1.50(±0.21) 10^{-4}·$Nm^{-1}K^{-1}$. Starting on the left side in Fig. 11, there appears to be the tendency for γ_T to slightly decrease for x_{Al}^{B} < 40 at.-% and increases for higher Al concentrations, which corresponds to the Butler model. However, this tendency is beyond the scatter of the experimental data.

The measured values and the values calculated from the Chatain and Butler model of the excess surface tension, γ^E, using Eq. (18), evaluated at a fixed temperature, T=1950 K (1677 °C), are shown in Fig. 12. The corresponding fit parameters, ${}^0u_{i,j}$ and ${}^1u_{i,j}$, for the excess surface tension of the measured data are listed in Tab. 7. The highest excess surface tension is found for $x_{Al}^{B} \leq 40$ at.-%, which amounts to 0.28 Nm^{-1}, while for higher Al concentrations the excess surface tension is significantly smaller, at around 0.1 Nm^{-1}. As seen in Fig. 7, both models are in good agreement with the surface tension, and the excess surface tension data, respectively. The Butler model underestimates the data, especially for $x_{Al}^{B} \leq 40$ at.-%, but reproduces the data within the error bars. The Chatain model overestimates the data, except for x_{Al}^{B} > 80 at.-%, and lies within the error bars, except for x_{Al}^{B}≈ 50-60 at.-%. Qualitatively, the Chatain model appears to reproduce the data more accurately for $x_{Al}^{B} \leq 40$ at.-%, while the Butler model appears more accurate for x_{Al}^{B} > 40 at.-%. The data and the Butler model

546 could indicate that a pronounced suppression of Al segregation only occurs up to a certain Al
547 concentration, of around 40 at.-%.
548 In Fig. 13 the isothermal surface tension data of the binary Al-Ti system, at *T*=1950 K (1677
549 °C), and literature surface data of pure Titanium and, some industrially used, multicomponent
550 alloys at equivalent temperatures, are plotted versus the Al concentration. As mentioned
551 above, multicomponent alloys on the basis of Al-Ti are of particular technical importance,
552 while data on their properties are sparse. As can be seen in Fig. 13, the surface tension data of
553 the binary system and the multicomponent alloys are in good agreement with deviations up to
554 10 %, in the case of $Al_6Ti_{90}V_4$, reported by Egry et al. [59]. Those deviations lie within the
555 same range of order as the relative uncertainties for the data of the pure e.g. 8 % for Ti, and
556 binary components e.g. 24 % for $Al_{80}Ti_{20}$, reported by Novacovic et al. [25] and in the present
557 work. Therefore, the data that are presented in the present work do not only fill the database
558 for thermophysical properties of binary Al-Ti alloys, but also established a good starting point
559 for investigations and processing of industrially used Al-Ti-based alloys with multiple
560 components.
561 Oxygen adsorption at the surface of the sample can produce a reduction in the surface tension.
562 The electromagnetic levitation technique is a generally clean method which avoids contact
563 between the liquid alloy and a container. Although it does not avoid contact with the gas
564 phase, an oxygen-reduced sample surface can still be achieved as discussed above. For the
565 surface tension of pure Ti, no comparable results for measurements under oxygen reduced
566 atmosphere are available. Anyhow, the mean value of the surface tension value for pure Ti of
567 this work is higher than the mean value of the cited literature data. That indicates that our
568 measurements are averagely and comparatively less affected by oxygen impurities.
569 For future works an extend study on the dependence of the surface tension on the oxygen
570 partial pressure of Al-Ti alloys would be of great value and interest. Such a study is presently
571 being carried out by us.

5. Summary

Density and surface tension of binary Al-Ti-alloys are measured over a broad temperature and composition range. It is found that, for all compositions, the density and surface tensions increase linearly upon decreasing temperatures. The data are analyzed concerning the temperature coefficients, excess molar volume, excess surface tension and surface segregation. Generally, Al-Ti is a highly nonideal system. Significantly highly negative values are found for the excess molar volume, which is in good agreement with other binary Ti-containing systems. Referring to the Al-Au system [34], shrunk Al radii are suggested to mainly trigger that mechanism, but further investigations are needed to verify this hypothesis. Concerning the surface tension, a highly nonideal behaviour could also be observed, with positive values for the excess surface tension. The results correspond well with the predictions of the Butler [39] and the Chatain model [44, 45] for nonideal solutions with excess free energy, ${}^{E}G \neq 0$. For nonideal solutions the models not only take the surface segregation of the surface active component, Al, into account, but also the suppression of the latter, due to interatomic attractions. Both mechanisms can be distinguished in the Al-Ti-system, coinciding with other Al-systems, reported by Brillo [24].

Overall, the nonideal behaviour for all investigated properties of the Al-Ti-system is more distinct for relatively low temperatures, due to the minor atomic dynamics and thus, enhanced interactions between atoms.

Multicomponent Al-Ti-based alloys - rather than binary Al-Ti-alloys - are of primary interest for various high temperature applications; however data on their properties are sparse. Before investigating partly highly complicated multi-component systems, it is an useful if not necessary approach to start with measurement in the binary system. In this work we could show that the data of the binary and multiple component systems are in very good agreement (Fig. 13). Therefore, we suggest that the data of the binary Al-Ti-system, presented in this

work, is not only interesting as fundamental research results, but may also be sufficient for many applications with multi-component Al-Ti-alloys.

Acknowledgments

This work has been supported by Professor Rainer Schmid-Fetzer, from TU-Clausthal, Institute of Metallurgy, who calculated the respective liquidus temperatures of the binary Al-Ti-system. The authors are grateful to Prof. Dr. Dieter Herlach for his critical review of this study and for his valuable suggestions.

606 **References**

607 [1] I. Egry, R. Brooks, D. Holland-Moritz, R. Novakovic, T. Matsushita, E. Ricci, S.
608 Seetharaman, R. Wunderlich, D. Jarvis, Int. J. Thermophys. 2007 vol. 28, pp. 1026-
609 1036

610 [2] Y.V. Naidich, Prog. Surf. Membr. Sci. 1981, vol. 14, pp. 353-484

611 [3] J.P. Garandet, B. Vinet, P. Gros, J. Colloid, Interf. Sci. 1994, vol. 165, pp, 351-354

612 [4] E. Gebhardt, M. Becker, S. Dorner, Aluminium 1955, vol. 31, pp. 315-321

613 [5] W. Coy, R. Mateer, Trans Amer. Soc. Metals, 1955, vol. 58, pp. 99 - 102

614 [6] E. Levin, G. Ayushina, P. Geld, High Temp. 1968, vol. 6 pp. 416-418

615 [7] A. Yatsenko,V. Kononenko, A. Sukhman, High Temp. 1972, vol. 10, pp. 55

616 [8] P. Smith, J. Elmer, G. Gallegos, Scripta Mat. 1999, vol. 40, pp. 937 - 941

617 [9] P. Nasch, S.G Steinemann, Phys. Chem. Liq. 1995, vol. 29, pp. 43-58

618 [10] K. Mills: Recommended values of thermophysical properties for selected commercial
619 alloys. Woodhead, Cambridge, 2002.

620 [11] M. Assael, R. Banish, J. Brillo, I. Egry, R. Brooks, P. Quested, K. Mills, A. Nagashima,
621 Y. Sato, W. Wakeham, J. Phys. Chem. Ref. Data, 2006, vol. 35, pp. 285-300

622 [12] T. Ishikawa, P. Paradis, J. Electron. Mater. 2005, vol. 34, pp. 1526-1532

623 [13] P. Paradis, T. Ishikawa, S. Yoda, Adv. Space Res. 2008, vol. 41, pp. 2118 - 2125

624 [14] G. Pottlacher: High Temperature Thermophysical Properties of 22 Pure Metals, Edition
625 Keiper, Graz, 2009.

626 [15] V.P. Elyutin, M.A. Maurakh, Izv. A.N., O.T.N. (USSR) 1955, vol. 6, pp. 129-131.

627 [16] V. Arkhipkin, A. Agaev, G. Grigorev, V. Kostikov, Ind. Lab. 1973, vol. 39, pp. 1340

628 [17] T. Ishikawa, P. Paradis, T. Itami, S. Yoda, J. Chem. Phys. 2003, vol. 118, pp. 7912-
629 7920

630 [18] B. Vinet, L. Magnusson, H. Fredriksson, P. Desre, J. Colloid Interface Sci. 2002, vol.
631 255, pp. 363–374

[19] K. Man, Int. J. Thermophys. 2000, vol. 21, pp. 793–804

[20] J. Tiele, J. Kelly, Brit. J. Appl. Phys. 1963, vol. 14, pp. 717–719

[21] B. Allen, Trans. Metall. Soc. AIME 1963, vol. 227, pp. 1175–1183

[22] A.W. Peterson, H. Kedesdy, P.H. Keck, E. Schwarz, J. Appl. Phys. 1958, vol. 28, pp. 213-216

[23] G. Kuppermann: The determination of the surface tension with the help of the levitated reciprocating drop under terrestrial conditions and in space. Dissertation Technology University of Berlin, 2000.

[24] J. Brillo: Thermophysical properties of multicomponent liquid alloys, Walter de Gruyter GmbH, Berlin/Boston, 2016.

[25] R. Novakovic, D. Giuranno, E. Ricci, A. Tuissi, R. Wunderlich, H.J. Fecht, I. Egry, Appl. Surf. Sci. 2012, vol. 258, pp. 3269–3275

[26] S. Amore, S. Delsante, H. Kobatake, J. Brillo, J. Chem. Phys. 2013, vol. 139, p. 064504

[27] S. Amore, J. Brillo, R. Novakovic, I. Egry, Appl. Surf. Sci. 2011, vol. 257, pp. 7739–7745.

[28] Y. Plevachuk, I. Egry, J. Brillo, D. Holland-Moritz, I. Kaban, Int J Mat Res. 2007, vol. 98, pp. 107–111

[29] I. Egry, J. Brillo, D. Holland-Moritz, Y. Plevachuk, Mat. Sci. Eng. 2008, vol. A 495, pp. 14- 18.

[30] J. Brillo, I. Egry, J. Westphal, Int. J. Mat. Res. 2008, vol. 99, pp. 162-167

[31] J. Schmitz, J. Brillo, I. Egry, R. Schmid-Fetzer, Int. J. Mat. Res. 2010, vol. 100, pp. 1529-1535

[32] J. Brillo, R. Brooks, I. Egry, P. Quested, High Temp.-High Press. 2008, vol. 37, pp. 371–381

[33] J. Brillo, Y. Plevachuk, I. Egry, J Mater Sci 2010, vol. 45, pp. 5150–5157

[34] H.L. Peng, T. Voigtmann, G. Kolland, H. Kobatake, J. Brillo, Phys. Review 2015, vol. B 92, pp. 184201-1 - 184201-13

[35] J. Brillo, G. Kolland, J. Mat. Sci. 2016, vol. 51, pp. 4888-4901

[36] J. Schmitz, B. Hallstedt, J. Brillo, I. Egry, M. Schick, J. Mater. Sci. 2012, vol. 47, pp. 3706–3712

[37] H. Kobatake, J. Brillo, J. Schmitz, P. Pichon, J. Mater. Sci. 2015, vol. 50, pp. 3351–3360

[38] H. Kobatake, J. Schmitz, J. Brillo. J. Mater. Sci. 2014, vol. 49, pp. 3541–3549

[39] J.A.V. Butler, Proc. R. Soc. 1932, vol. A135, pp. 348–374

[40] G. Kaptay, Calphad 2008, vol. 32, pp. 338–352

[41] T. Tanaka, T. Iida, Steel Res. 1994, vol. 65, pp. 21–28

[42] T. Tanaka, K. Hack, T. Iida, S. Hara, Z. Metallkd. 1996, vol. 87, pp. 380-389

[43] G. Kaptay, Langmuir 2015, vol. 31, pp. 5796–5804

[44] P. Wynblatt, A. Saul, D. Chatain, Acta Mater 1998, vol. 46, pp. 2337–2347

[45] C. Antion, D. Chatain, Surf. Sci. 2007, vol. 10, pp. 2232–2244

[46] I. Egry, J. Brillo, High Temperatures – High pressures 2013, vol. 42, pp. 59-68

[47] J. Brillo, G. Lohöfer, F. Schmidt-Hohagen, S. Schneider, I. Egry, Int. J. Materials and Product Technology 2006, vol. 26, pp. 247-273

[48] W. Wien, Philos. Magaz. 1897, vol. 5, pp. 214–220

[49] S. Krishnan, G.P. Hansen, R.H. Hauge, J.L. Margrave, High Temp. Sci. 1990, vol. 29, pp. 17- 52

[50] V. Witusiewicz, A.A. Bondar, U. Hecht, S. Rex, T. Velikanova, J. All. and Comp. 2008, vol. 465, pp. 64–77

[51] J. Brillo, I. Egry, Int. J. Thermophys. 2003, vol. 24, pp. 1155-1170.

[52] D.L. Cummings, D.A. Blackburn, J. Fluid Mech. 1991, vol. 224, pp. 395-416

[53] P. Paradis, W.K. Rhim, J. Chem. Thermodynamics 2000, vol. 32, pp. 123–133

[54] JM. Molina, R. Voytovych, E. Louis, N. Eustathopoulos, Int J Adh Adhesives 2007, vol. 27, pp. 394–401

[55] H. Ellingham, J. Soc. Chem. Ind. 1944, vol. 63, pp. 125 - 133

[56] N. Eustathopoulos, B. Drevet, J Crys Growth 2013, vol. 371, pp. 77–83

[57] L. N. Belyanchikov, Elektrometallurgiya 2009, vol. 11, pp. 25-32

[58] M.W. Chase, C.A. Davies, J.R. Downey, D.J. Furip, R.A. McDonald, A.N. Syverud, J. Phys. Chem. Ref. Data 1985, vol. 14, Suppl 1, pp. 1-1856

[59] I. Egry, D. Holland-Moritz, R. Novakovic, E. Ricci, R. Wunderlich, N. Sobczak, Int. J. Thermophys. 2010, vol. 31, pp. 949–965

[60] R. Nowak, T. Lanata, N. Sobczak, E. Ricci, D. Giuranno, R. Novakovic, D. Holland-Moritz, I. Egry, J. Mater. Sci. 2010, vol. 45, pp. 1993–2001

Figure captions:

Fig. 1: Scheme of the phase diagram of **Al-T**i according to the thermodynamic description of Witusiewicz et al. using the CALPHAD approach [50]. For the sake of clarity, details at low temperature have been omitted.

Fig. 2: Measured density, ρ, of liquid Al-Ti (symbols) and their linear fits (lines) versus temperature, T, following Eq. (1). For the pure elements the fits for the mean values of all measurements of Al and Ti are shown. The inset shows a magnified portion of the figure for Al-mole fractions $x_{\mathrm{Al}}^{\mathrm{B}}$, ranging from 10 to 50 at.-%.

Fig. 3: Molar volumes in dependence of the mole fraction, $x_{\mathrm{Al}}^{\mathrm{B}}$ of measurements at T=1873 K (solid circles), molar volumes extrapolated to a temperature range below (hollow circles) and above (half-solid circles) measurement conditions. The lines show the ideal molar volumes (dotted line) and fitted molar volumes with one fit parameter, ${}^{0}V$, (solid line) and two fit parameters, ${}^{0}V$ and ${}^{1}V$, (dashed-dotted-dotted line), following Eq. (4, 5).

Fig 4: Surface tension of pure liquid Al as function of temperature. The circles denote data measured by Kolland [35] and the squares data measured by Kobatake [36] under oxygen reduced conditions. The solid and the dashed-dotted lines represent corresponding fits to this data. For comparison, representations of the surface tension data of Molina [54] are shown by the dashed and dotted lines.

Fig. 5: Surface tension of liquid Ti (solid symbols) versus temperature. For comparison, data of various authors are shown as well (hollow symbols). The long dashed line represents our previous results determined in EML [27] and the results obtained by Paradis [53] using electrostatic levitation are represented by the dashed-double-dotted line.

Fig. 6: Literature surface tension, γ, of liquid Al [24, 35] and measured surface tension of liquid Al-Ti (symbols) and their linear fits (lines) in dependence of temperature, T, following

719 Eq. (8). The inset shows a magnified portion of the figure for Al-mole fractions $x_{\mathrm{Al}}^{\mathrm{B}}$, ranging
720 from 0 to 40 at.-%.
721 **Fig. 7:** Isothermal surface tension γ of measured liquid Al-Ti and literature data for pure
722 liquid Al, in dependence of the bulk mole fraction $x_{\mathrm{Al}}^{\mathrm{B}}$ at 1950 K (1677 °C). The squares
723 show the extrapolated measured surface tension data, the lines represent the data fit with two
724 fit parameter, ${}^{0}u$ and ${}^{1}u$, (dashed-dotted-dotted line) following Eq. (21), surface tension values
725 calculated with the Butler model [39] for subregular solutions with ideal (dotted line) and
726 nonideal mixing behaviour (dashed line) and the Chatain model [44,45] for subregular
727 solutions (solid line), as described in the text.
728 **Fig. 8:** Fitted excess molar volumes, V^{E} (Eq. 15), of first order fits $(\mathrm{N} = 1)$ at T=1473 K
729 (1200 °C) (dotted line), 1673 K (1400 °C) (dashed line) and 1873 K (1600 °C) (solid line).
730 **Fig 9:** Calculated surface mole fraction $x_{\mathrm{Al}}^{\mathrm{S}}$ as a function of the bulk mole fraction $x_{\mathrm{Al}}^{\mathrm{B}}$ at
731 T=1950 K (1677 °C) using the ideal (dotted line) and nonideal (dashed line) subregular
732 solution model by Butler [39] and by Chatain [44,45] (solid lines) for different layers, where
733 layer "1" denotes the layer at the surface. The layer numbers increase with their distance to
734 the surface.
735 **Fig 10:** Calculated surface mole fraction $x_{\mathrm{Al}}^{(\mathrm{n})}$ as a function of the bulk mole fraction $x_{\mathrm{Al}}^{\mathrm{B}}$ at
736 T=1700 K (1477 °C) (triangles) and T=1950 K (1677 °C) (squares) using the nonideal
737 subregular solution model by Chatain [44, 45] for different layers, where the layer numbers
738 increase with their distance to the surface.
739 **Fig 11:** Temperature coefficient values γ_{T} (Eq. (8) in dependence of the bulk mole fraction
740 $x_{\mathrm{Al}}^{\mathrm{B}}$ of measured data at 1950 K (1677 °C), represented by the squares. The lines represent the
741 calculated temperature coefficient values for the nonideal subregular solution model by Butler
742 [39] (dashed line) and by Chatain [44, 45] (solid line).

Fig 12: Isothermal excess surface tension γ^E of liquid Al-Ti as a function of the bulk mole fraction $x_{\mathrm{Al}}^{\mathrm{B}}$ at T=1950 K (1677 °C). The symbols show the extrapolated measured surface tension data substracted by the calculated surface tension values of the Butler [39] (squares) and Chatain [44, 45] (triangles) model for ideal subregular solutions. The lines represent excess surface tension γ^E, (Eq. (20)), values calculated as the difference between the Butler (dashed line) and Chatain (solid line) model for ideal and nonideal subregular solutions.

Fig. 13: Surface tension γ of liquid Al-Ti in dependence of the bulk mole fraction $x_{\mathrm{Al}}^{\mathrm{B}}$ of measured data at 1950 K (1677 °C) and of Ti and industrially used Al-Ti-based alloys at similar temperatures: Tiele [20], Allen [21], Amore [27], Arkhipkin [16], Paradis [17,52] Kuppermann [23] Man [19], Nowak [60] Novakovic [25] and Egry [1,59].

Table captions:

Table 1: Key of methods for the density and surface tension data, selected from literature and as used in the tables 2 and 7. The key R, meaning "recommended", species that the listed value is obtained from a literature review.

Table 2: Parameters T_L, ρ_L, and ρ_T and the interpolated density $\rho(T$=1873 K (1600 °C)) and its mean values in bold font of pure liquid Al and Ti.

Table 3: Parameters T_L, ρ_L, and ρ_T and the extrapolated density $\rho(T$=1873 K (1600 °C)) of the investigated liquid alloys Al_xTi_{100-x}.

Table 4: Parameters γ_L, and γ_T and the extrapolated isothermal surface tension $\gamma(T$=1950 K (1677 °C)) and its mean values in bold font for liquid Ti measured in this work and the selected data from literature for liquid Al used for the models and the references, respectively.

Table 5: Parameters γ_L, and γ_T and the interpolated surface tension $\gamma(T$=1950 K (1677 °C)) of the investigated liquid alloys Al_xTi_{100-x}.

Table 6: Parameters T_L and ρ_L and its mean values in bold font for the density of pure Al and Ti selected from literature. The methods and references are specified in the fourth and fifth column and the method key can be found in Tab. 3.

Table 7: Coefficients ${}^{v}V$(T) of Redlich-Kister type polynomial fit, following Eq. (5) for fitted excess molar volumes, V^E, temperature dependent parameters ${}^{v}L$ used for the calculations of the subregular solution models by Butler and by Chatain (Eq. (15) and coefficients ${}^{v}u$(T) of

Table 8: Compilation of surface tension values γ_L and γ_T and the corresponding references and methods for liquid Titanium. The method key is listed in Tab. 3, respectively. Redlich-Kister type polynomial fit following Eq. (21) for fitted excess surface tension, γ^E.

Table 1

Key	Method
CR	Rise method
DC	Draining crucible
ESL	Electro static
DW	Drop weight
PW	Pedant wire
EML	Electro magnetic
OD	Oscillating drop
PD	Pendant drop
A	Archimedian methods
BP	Bubble Pressure
SD	Sessile drop
G	γ-Absorption dilatometry
EW	Exploding wire
R	Recommended from literature review

Table 2

Composition	T_L (K (°C))	ρ_L (gcm^{-3})	ρ_T ($10^{-4}gcm^{-3}K^{-1}$)	ρ(T=1873K (1600 °C)) (g/cm^3)
Ti	1941 (1668)	4.14	-1.48	4.15
Ti	1941 (1668)	4.15	-4.4	4.18
Ti	1941 (1668)	4.06	-3.14	4.08
Ti	1941 (1668)	4.13	-2.38	4.14
Ti	**1941 (1668)**	**4.12±0.04**	**-2.85±1.23**	**4.14±0.04**
Al	933 (660)	2.32	-2.52	2.08
Al	933 (660)	2.28	-1.88	2.10
Al	933 (660)	2.29	-2.14	2.09
Al	**933 (660)**	**2.30±0.02**	**-2.18±0.32**	**2.09±0.01**

Table 3

Composition	T_L (K (°C))	ρ_L (gcm^{-3})	ρ_T ($10^{-4}gcm^{-3}K^{-1}$)	ρ(T=1873 K (1600 °C)) (g/cm^3)
$Al_{10}Ti_{90}$	1962 (1689)	3.91	-4.98	3.96
$Al_{10}Ti_{90}$	1962 (1689)	3.82	-2.78	3.84
$Al_{20}Ti_{80}$	1948 (1675)	3.63	-3.91	3.66
$Al_{20}Ti_{80}$	1948 (1675)	3.67	-3.17	3.69
$Al_{25}Ti_{75}$	1941 (1668)	3.69	-5.49	3.73
$Al_{25}Ti_{75}$	1941 (1668)	3.65	-3.37	3.67
$Al_{25}Ti_{75}$	1941 (1668)	3.61	-5.53	3.65
$Al_{30}Ti_{70}$	1915 (1642)	3.52	-7.57	3.55
$Al_{30}Ti_{70}$	1915 (1642)	3.53	-3.2	3.54
$Al_{40}Ti_{60}$	1853 (1580)	3.37	-1.18	3.36
$Al_{50}Ti_{50}$	1757 (1484)	3.34	-4.91	3.36
$Al_{50}Ti_{50}$	1757 (1484)	3.38	-4.51	3.32
$Al_{60}Ti_{40}$	1721 (1448)	3.13	-5.56	3.04
$Al_{70}Ti_{30}$	1689 (1416)	2.91	-3.53	2.85
$Al_{70}Ti_{30}$	1689 (1416)	2.88	-3.37	2.82
$Al_{80}Ti_{20}$	1654 (1381)	2.69	-5.82	2.57
$Al_{80}Ti_{20}$	1654 (1381)	2.69	-5.58	2.57
$Al_{90}Ti_{10}$	1562 (1289)	2.46	-3.41	2.36

Table 4

Element	T_L (K (°C))	γ_L (Nm^{-1})	γ_T ($10^{-4}Nm^{-1}K^{-1}$)	γ(T=1950 K (1677 °C)) (Nm^{-1})	Reference
Ti	1941 (1668)	1.56	-0.62	1.56	Present work
Ti	1941 (1668)	1.58	-2.49	1.57	Present work
Ti	1941 (1668)	1.54	-1.85	1.54	Present work
Ti	**1941 (1668)**	**1.56±0.02**	**-1.65±0.95**	**1.55±0.02**	
Al	933 (660)	0.98	-2.71	0.70	[37]
Al	933 (660)	0.87	-1.46	0.72	[35]
Al	**933 (660)**	**0.92±0.08**	**-2.09±0.88**	**0.71±0.02**	

Table 5

Composition	T_L (K (°C))	γ_L (Nm^{-1})	γ_T ($10^{-4}Nm^{-1}K^{-1}$)	$\gamma(T$=1950 K (1677 °C)) (Nm^{-1})
$Al_{10}Ti_{90}$	1962 (1689)	1.52	-4.34	1.53
$Al_{10}Ti_{90}$	1962 (1689)	1.46	-5.81	1.47
$Al_{20}Ti_{80}$	1948 (1675)	1.35	-3.29	1.35
$Al_{20}Ti_{80}$	1948 (1675)	1.28	-2.18	1.28
$Al_{25}Ti_{75}$	1941 (1668)	1.30	-2.42	1.30
$Al_{25}Ti_{75}$	1941 (1668)	1.36	-3.38	1.36
$Al_{30}Ti_{70}$	1915 (1642)	1.34	-3.38	1.33
$Al_{30}Ti_{70}$	1915 (1642)	1.33	-4.24	1.31
$Al_{40}Ti_{60}$	1853 (1580)	1.24	-1.79	1.23
$Al_{50}Ti_{50}$	1757 (1484)	1.07	-2.86	1.01
$Al_{60}Ti_{40}$	1721 (1448)	0.96	-0.68	0.95
$Al_{70}Ti_{30}$	1689 (1416)	0.94	-1.80	0.89
$Al_{80}Ti_{20}$	1654 (1381)	0.92	-1.61	0.88
$Al_{90}Ti_{10}$	1562 (1289)	0.89	-3.14	0.77
$Al_{90}Ti_{10}$	1562 (1289)	0.81	-0.23	0.80

Table 6

Composition	ρ_L (gcm^{-3})	ρ_T ($10^{-4}gcm^{-3}K^{-1}$)	Reference	Method
Al	2.37	-2.6	[35]	A
Al	2.39	-3.9	[36]	BP
Al	2.37	-2.6	[37]	SD
Al	2.38	-3.3	[38]	SD
Al	2.37	-3.1	[39]	G
Al	2.38	-2.3	[40]	G
Al	2.38	-2.3	[41]	R
Al	2.37	-3.1	[42]	R
Al	2.36	-3.3	[4]	EML
Al	2.36	-3.0	[4]	EML
Al	2.29	-2.5	[4]	EML
Al	**2.36±0.03**	**-2.91±0.50**		
Ti	4.17	-2.2	[43]	ESL
Ti	4.10	-9.9	[44]	ESL
Ti	4.21	-5.1	[52]	ESL
Ti	4.14	-2.25	[41]	R
Ti	4.29	-2.3	[45]	WE
Ti	4.1	-3.3	[4]	EML
Ti	**4.17±0.07**	**-4.18±3.02**		

Table 7

ν	${}^{\nu}V(T)$ (m^3mol^{-1})	${}^{\nu}L$ ($Jmol^{-1}$)	${}^{\nu}u(T)$ ($Nm^{-1}mol^{-1}$)
0	$0.00247T$-6.55516	$41.972T$-118048	$-0.00136T$+2.8091
1	$-0.001T$+4.3711	$19.704T$-23613	$-2.18327\cdot10^{-4}T$+0.21604
2		$-13.844T$+34757	

Table 8

γ_L (10^{-4} $Nm^{-1}K^{-1}$)	γ_T (10^{-4} $Nm^{-1}K^{-1}$)	T (K (°C))	Reference	Method
1.51	-	1940 (1667)	Elyutin et al. [15]	CR
1.41	-	1941 (1668)	Arkhipkin et al. [16]	DC
1.557	-0.156	1943 (1670)	Paradis et al. [17,52]	ESL
1.525	-	1943 (1670)	Vinet et al. [18]	DW/PW
1.475	-	1943 (1670)	Man et al. [19]	PD
1.49	-0.17	1943 (1670)	Brillo et al. [27]	EML-OD
1.588	-	1953 (1680)	Tiele et al. [20]	DW
1.65	-	1953 (1680)	Allen et al. [21]	PD
1.39	-	1953 (1680)	Peterson et al. [22]	PD
1.675	-	1953 (1680)	Kupperman et al. [23]	Levitation
1.58	-2.49	1941 (1668)	Present work	EML-OD
1.54	-1.85	1941 (1668)	Present work	EML-OD
1.56	-0.62	1941 (1668)	Present work	EML-OD

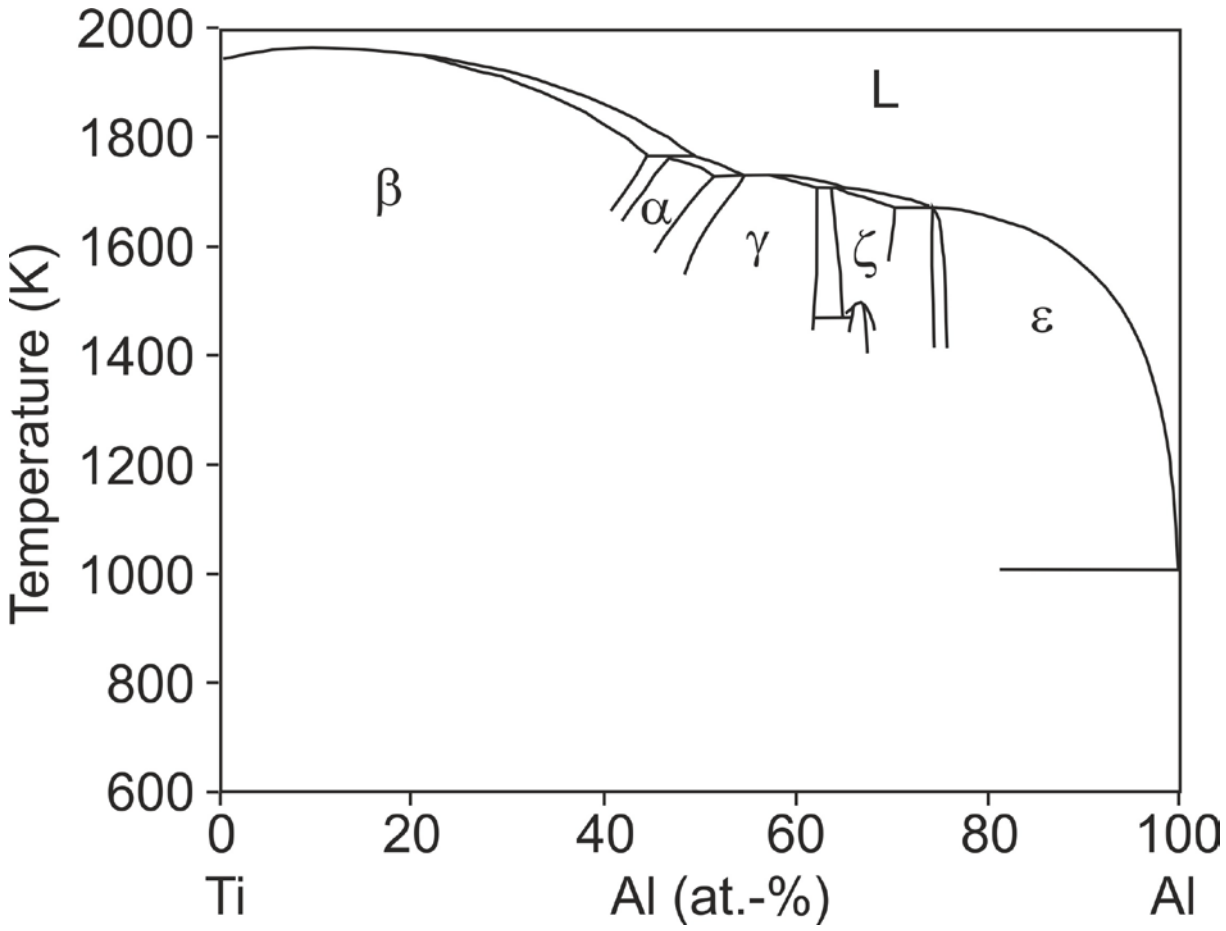
2000
1800
1600
1400
1200
1000
800
600
Temperature (K)
L
β
α
γ
ζ
ε
0
20
40
60
80
100
Ti
Al (at.-%)
Al

Figure 1

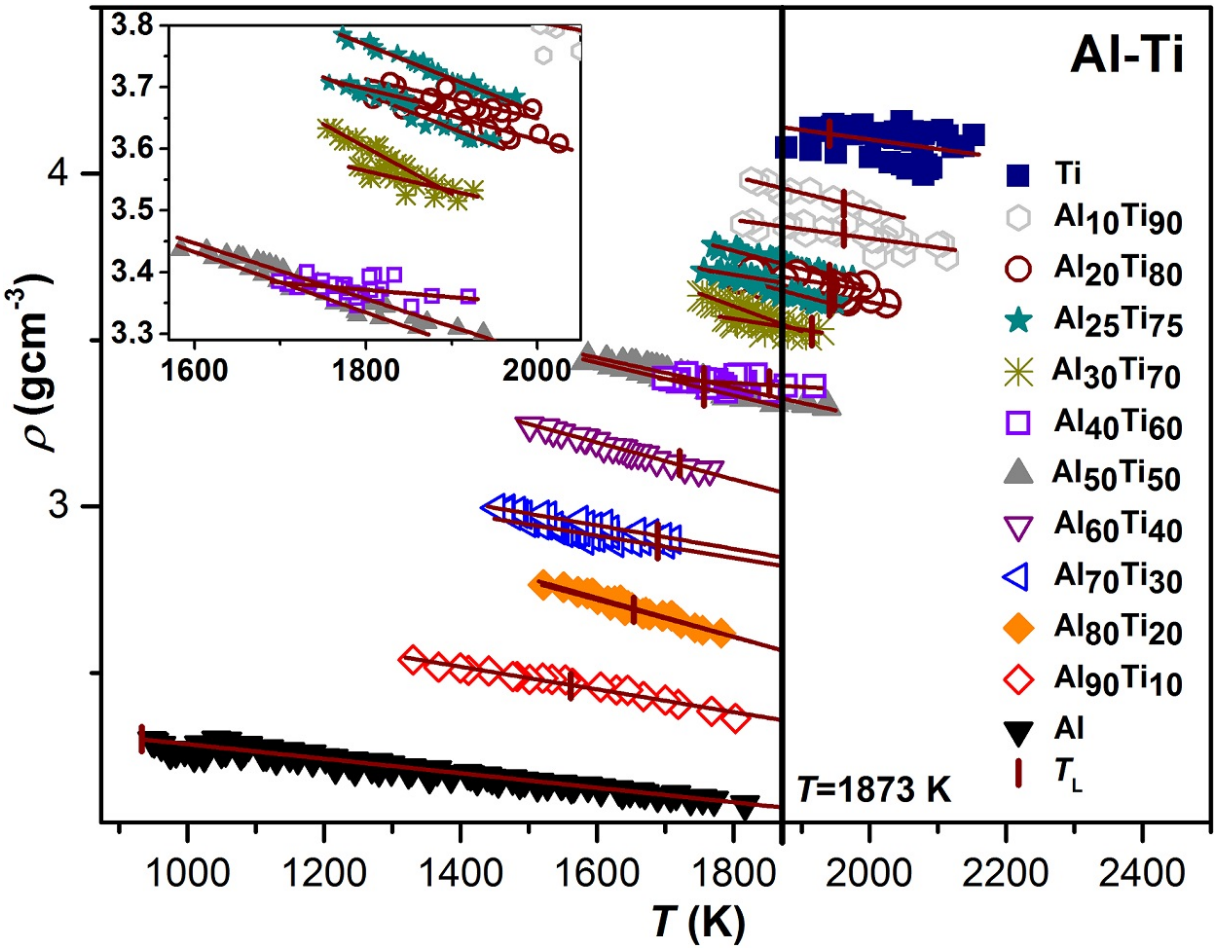
Al-Ti
Ti
Al10Ti90
Al20Ti80
Al25Ti75
Al30Ti70
Al40Ti60
Al50Ti50
Al60Ti40
Al70Ti30
Al80Ti20
Al90Ti10
Al
TL
T=1873 K
ρ (gcm-3)
T (K)
4
3
1000
1200
1400
1600
1800
2000
2200
2400
3.8
3.7
3.6
3.5
3.4
3.3
1600
1800
2000

Figure 2

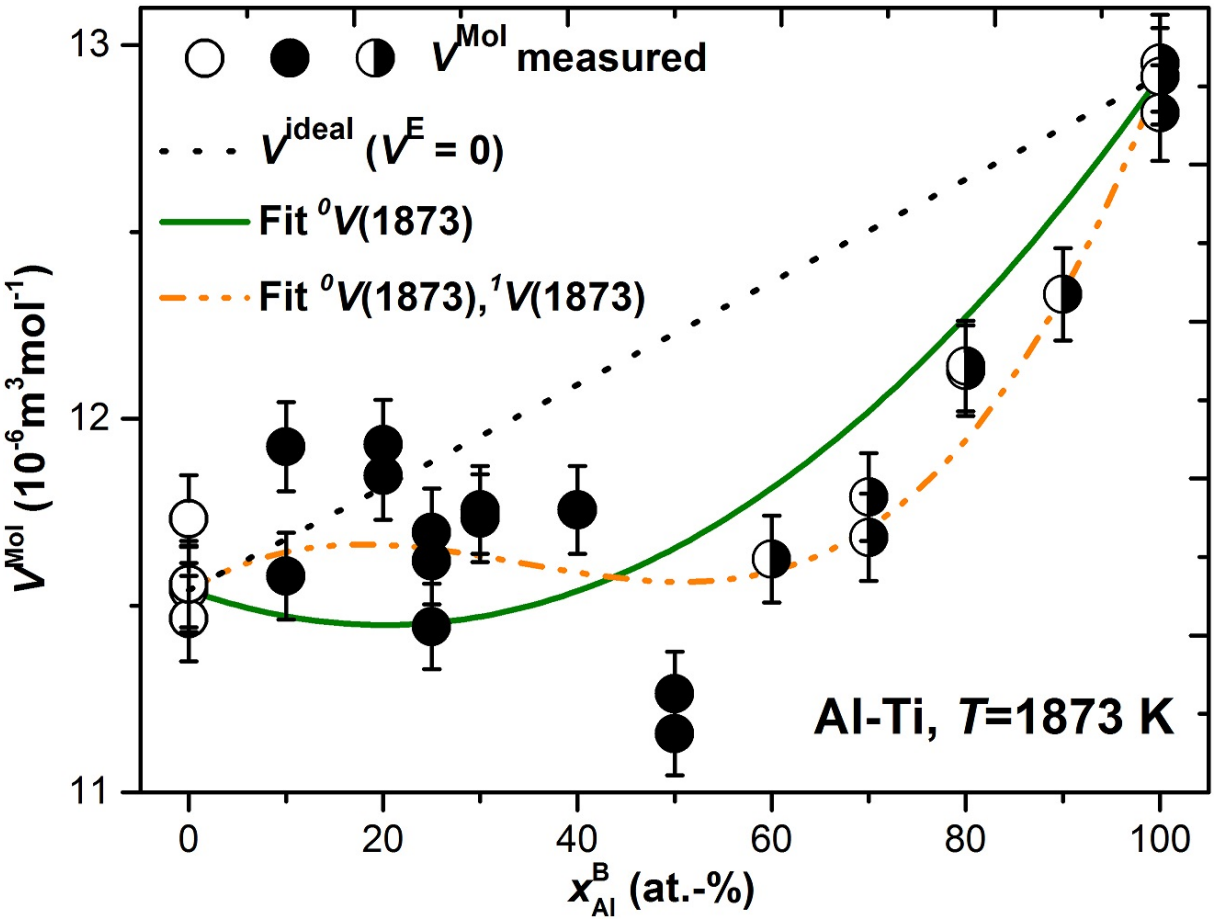
V^{Mol} measured
V^{ideal} (V^E = 0)
Fit ^0V(1873)
Fit ^0V(1873),^1V(1873)
Al-Ti, T=1873 K
V^{Mol} (10^{-6}m^{3}mol^{-1})
x^B_{Al} (at.-%)
13
12
11
0
20
40
60
80
100

Figure 3

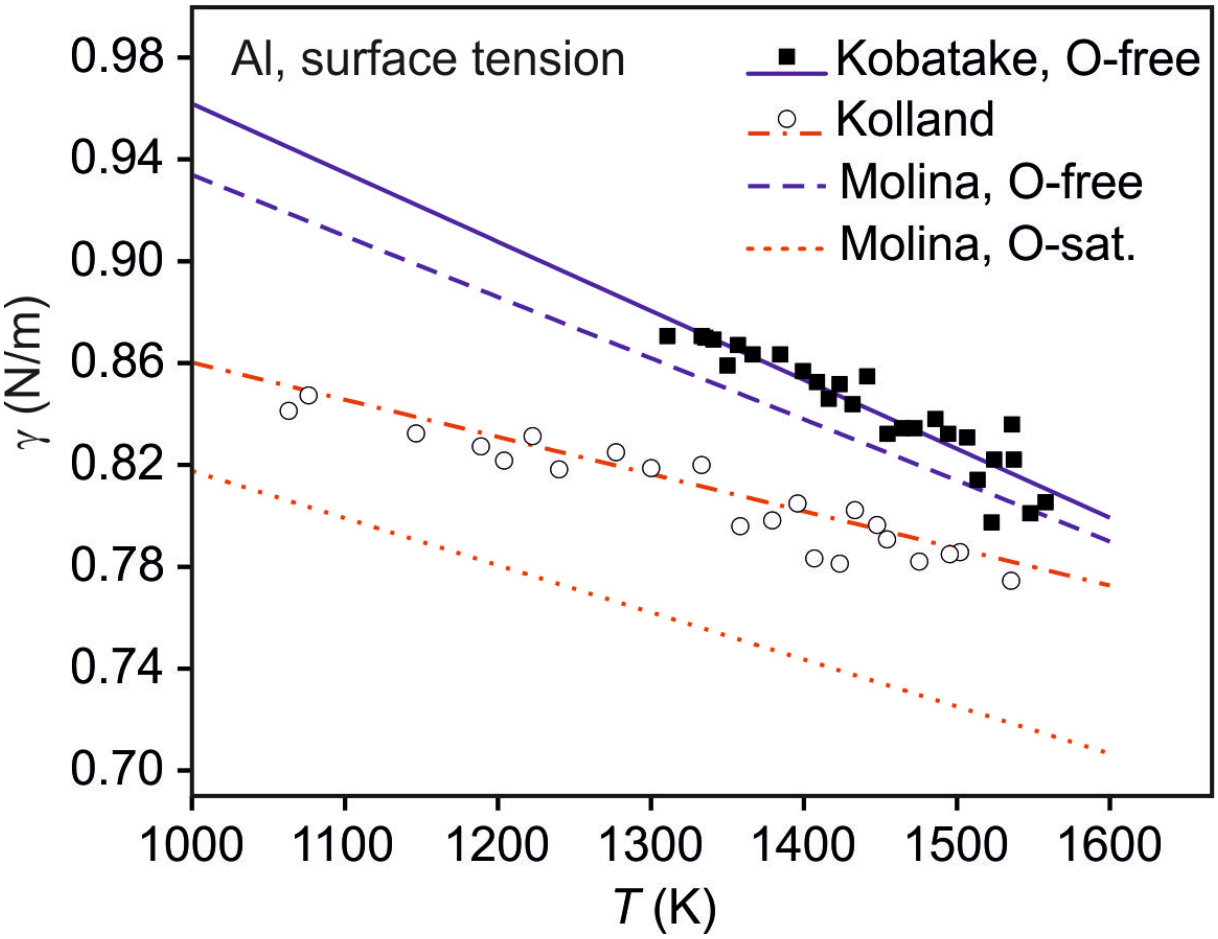
Al, surface tension
Kobatake, O-free
Kolland
Molina, O-free
Molina, O-sat.
γ (N/m)
0.98
0.94
0.90
0.86
0.82
0.78
0.74
0.70
1000
1100
1200
1300
1400
1500
1600
T (K)

Figure 4

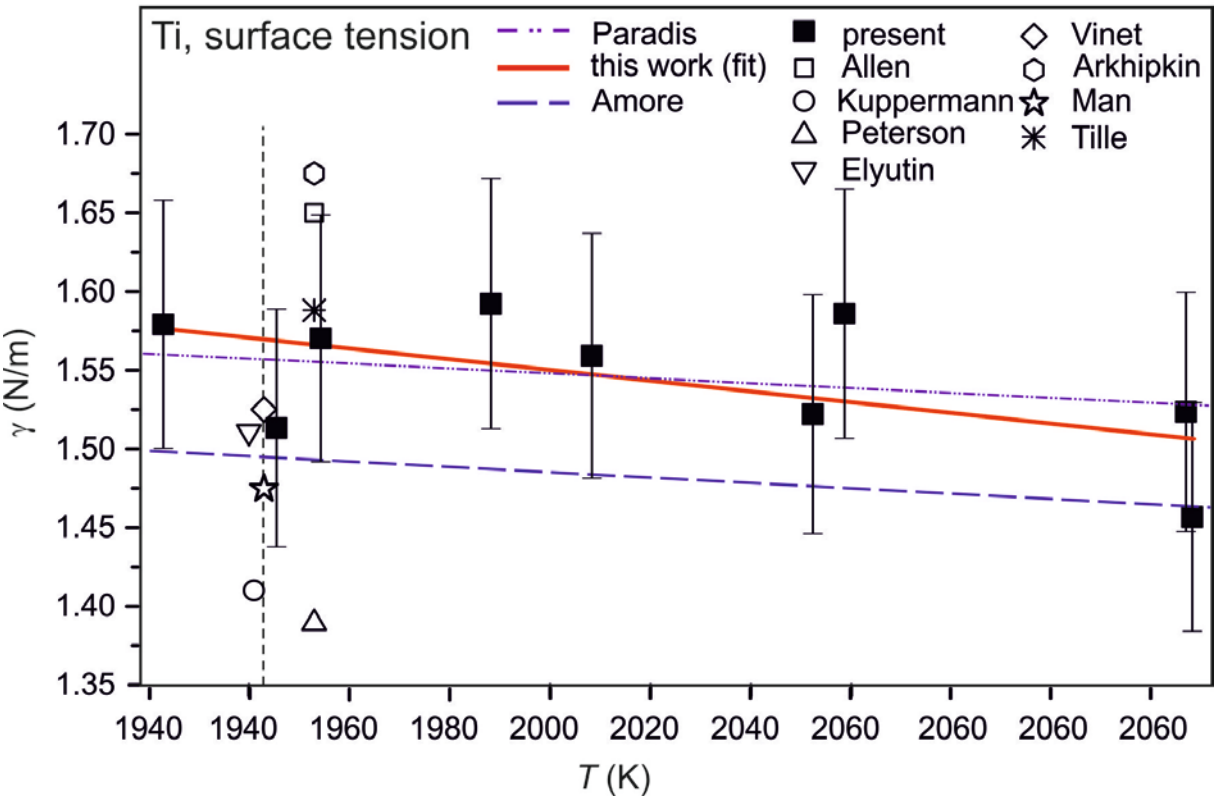
Ti, surface tension
Paradis
this work (fit)
Amore
present
Allen
Kuppermann
Peterson
Elyutin
Vinet
Arkhipkin
Man
Tille
γ (N/m)
1.70
1.65
1.60
1.55
1.50
1.45
1.40
1.35
1940
1940
1960
1980
2000
2020
2040
2060
2060
2060
2060
T (K)

Figure 5

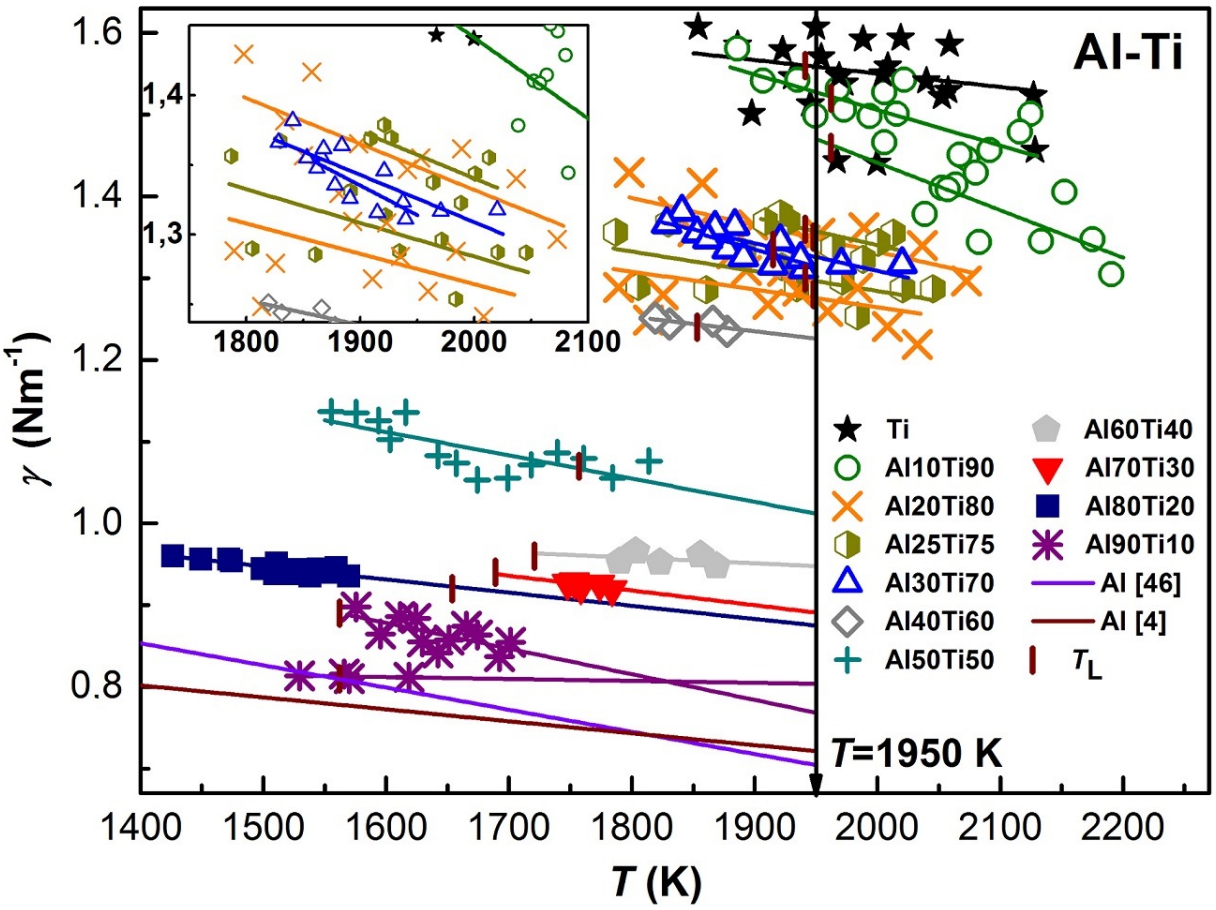
Al-Ti
γ (Nm-1)
T (K)
T=1950 K
Ti
Al10Ti90
Al20Ti80
Al25Ti75
Al30Ti70
Al40Ti60
Al50Ti50
Al60Ti40
Al70Ti30
Al80Ti20
Al90Ti10
Al [46]
Al [4]
TL

Figure 6

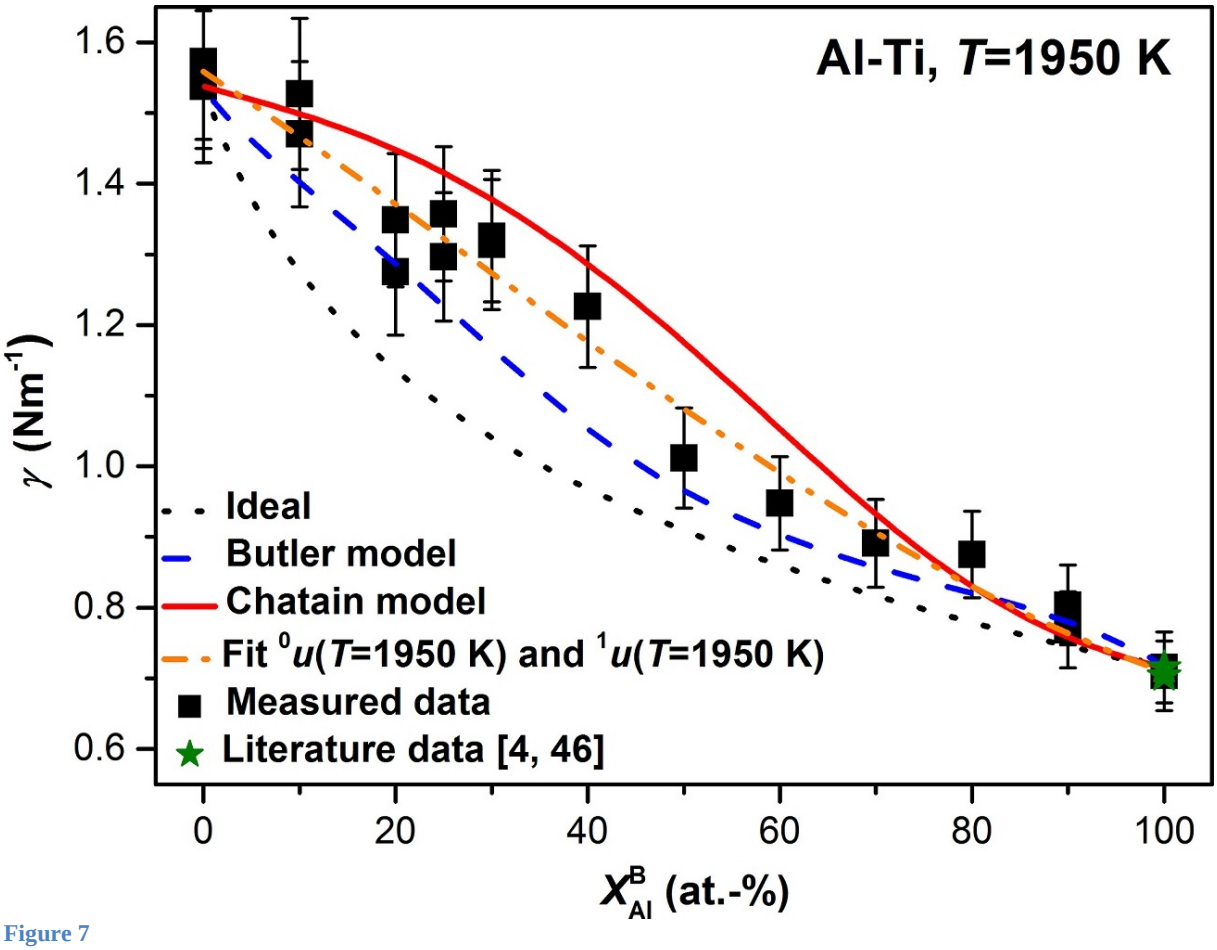
Al-Ti, T=1950 K
γ (Nm-1)
1.6
1.4
1.2
1.0
0.8
0.6
0
20
40
60
80
100
X_Al^B (at.-%)
Ideal
Butler model
Chatain model
Fit 0u(T=1950 K) and 1u(T=1950 K)
Measured data
Literature data [4, 46]

Figure 7

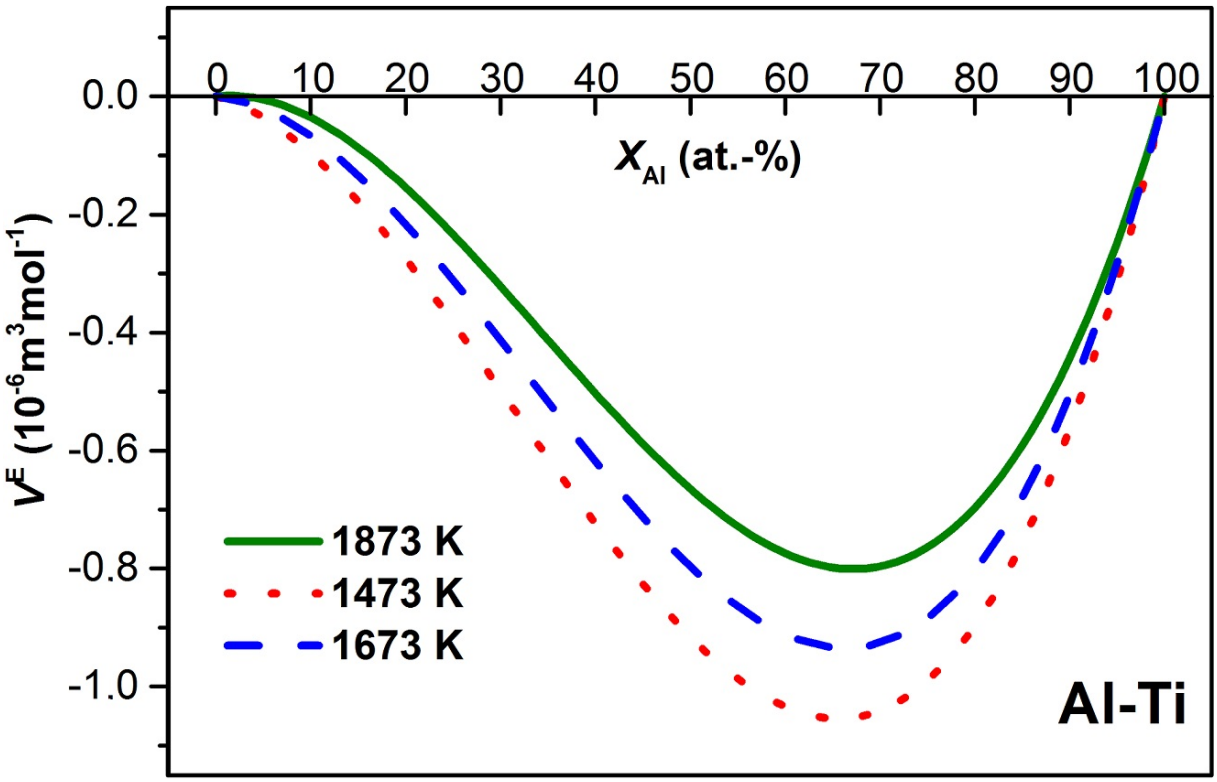
0
10
20
30
40
50
60
70
80
90
100
0.0
-0.2
-0.4
-0.6
-0.8
-1.0
X_{Al} (at.-%)
V^E ($10^{-6}m^3mol^{-1}$)
1873 K
1473 K
1673 K
Al-Ti

Figure 8

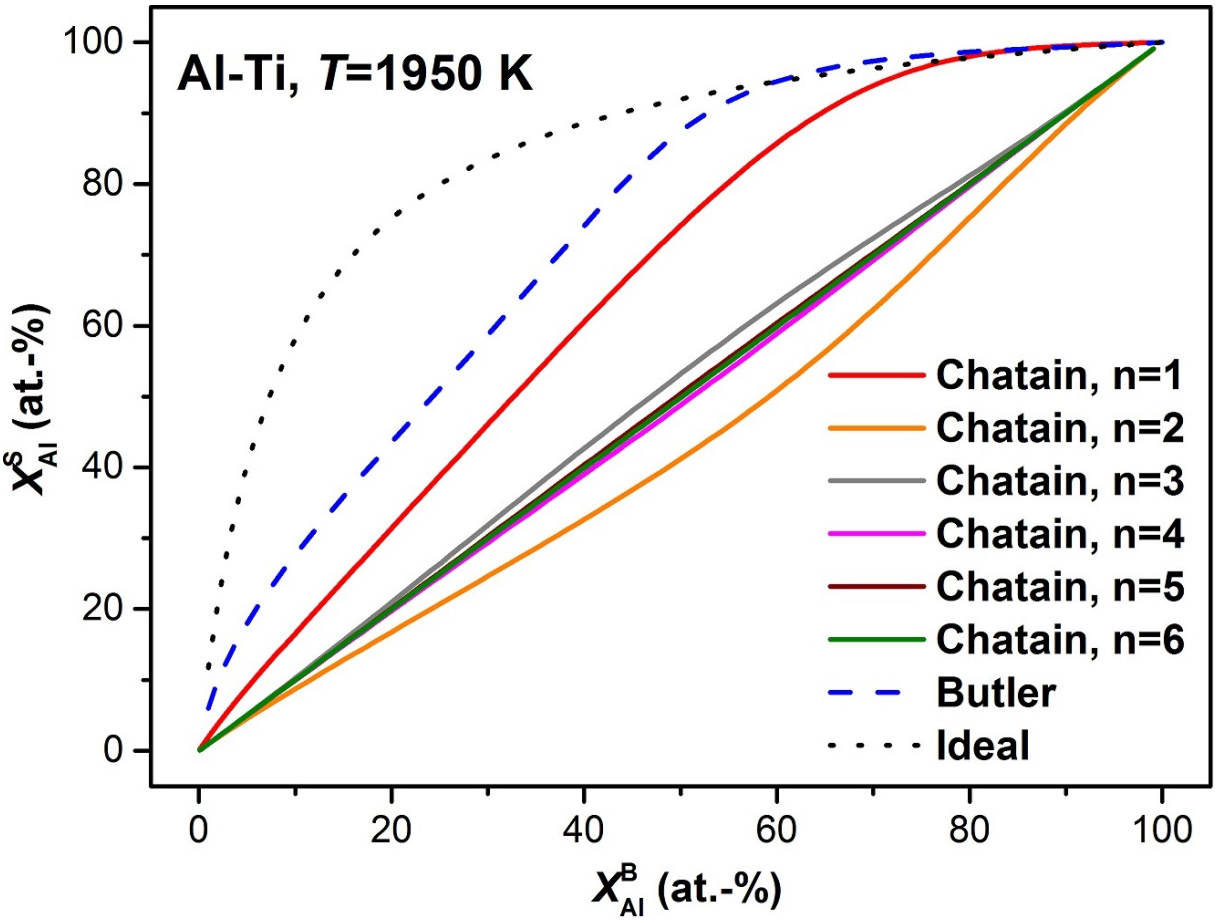
Al-Ti, T=1950 K
Chatain, n=1
Chatain, n=2
Chatain, n=3
Chatain, n=4
Chatain, n=5
Chatain, n=6
Butler
Ideal
X^S_{Al} (at.-%)
X^B_{Al} (at.-%)
0
20
40
60
80
100

Figure 9

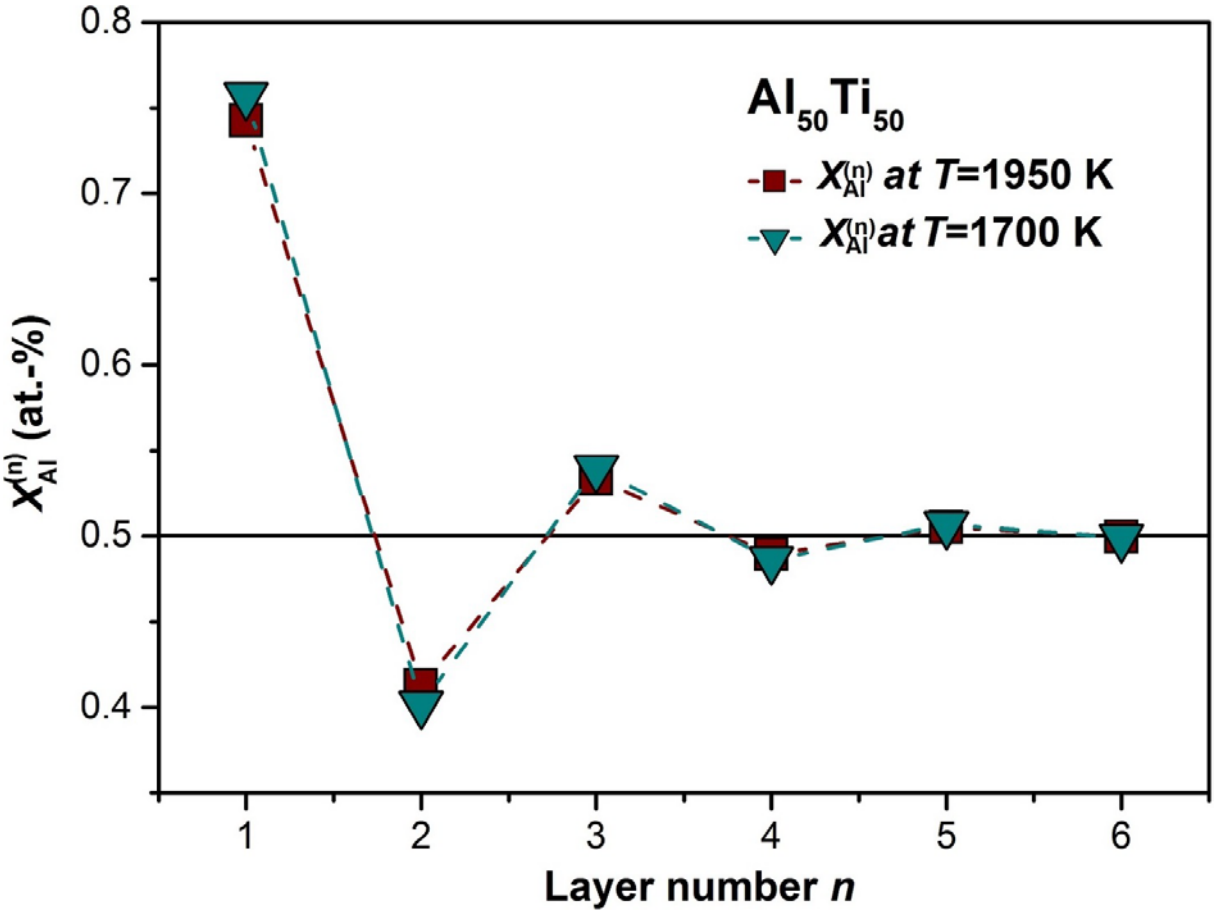
Al50Ti50
X(n)Al at T=1950 K
X(n)Al at T=1700 K
X(n)Al (at.-%)
Layer number n
0.8
0.7
0.6
0.5
0.4
1
2
3
4
5
6

Figure 10

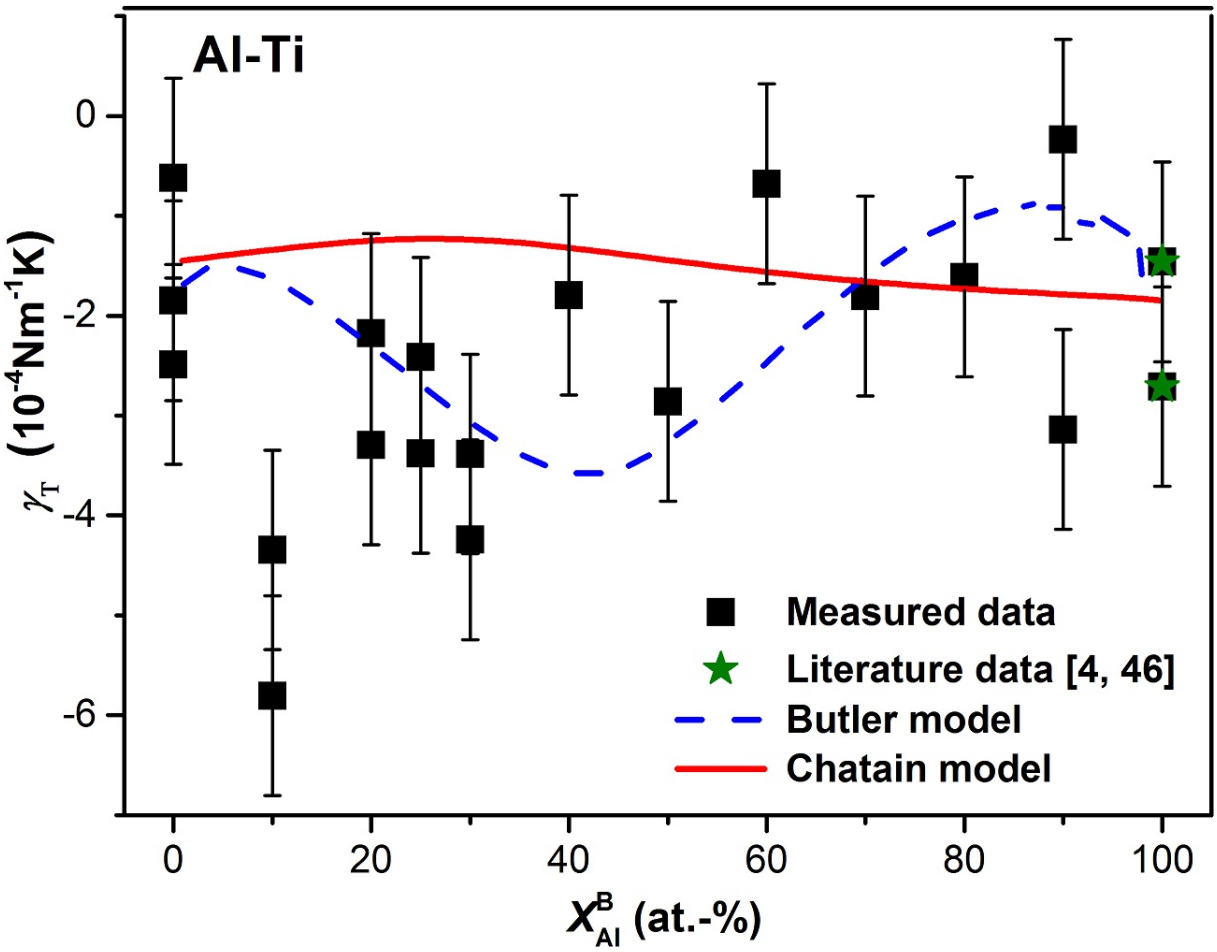
Al-Ti
0
-2
-4
-6
γ_T (10^{-4}Nm^{-1}K)
0
20
40
60
80
100
X_{Al}^{B} (at.-%)
Measured data
Literature data [4, 46]
Butler model
Chatain model

Figure 11

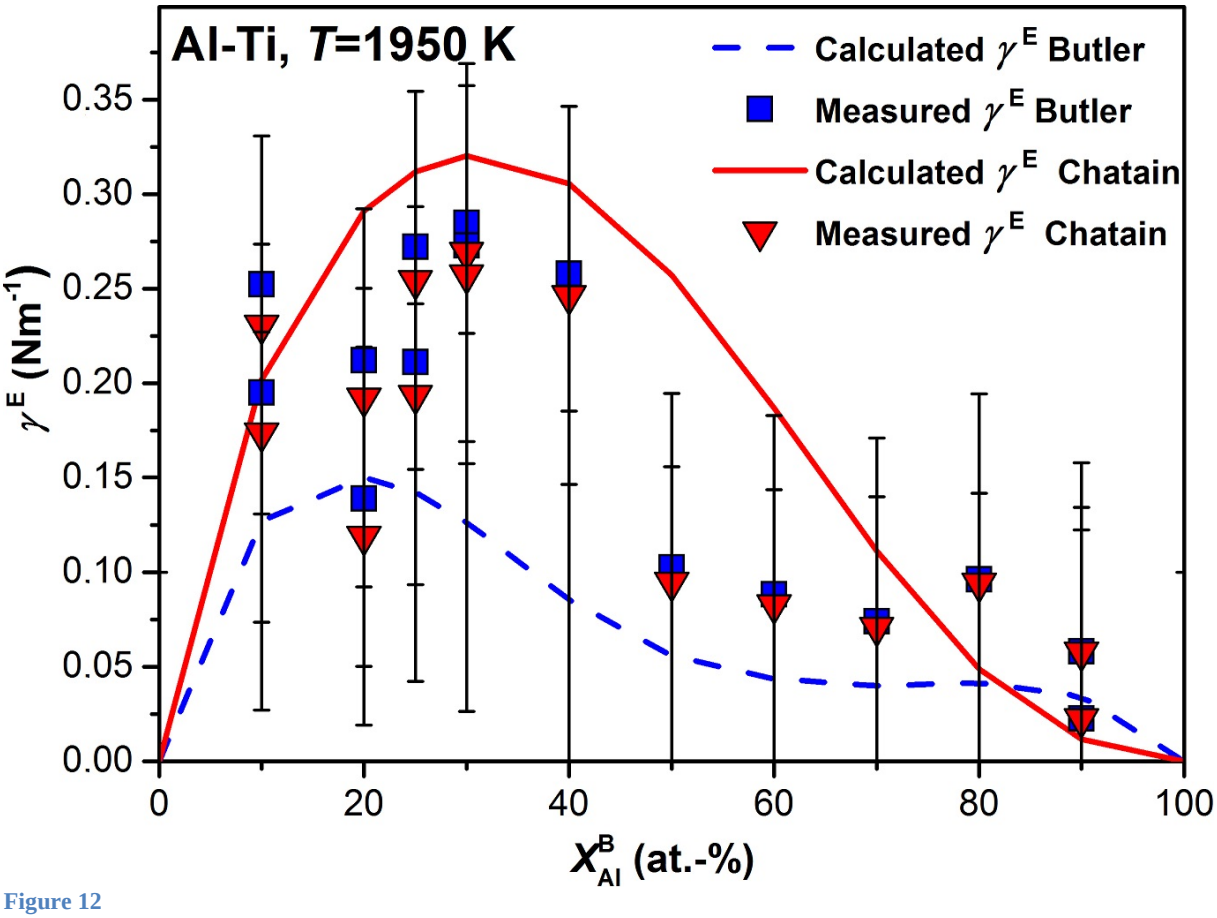
Al-Ti, T=1950 K
Calculated γ^E Butler
Measured γ^E Butler
Calculated γ^E Chatain
Measured γ^E Chatain
γ^E (Nm^-1)
0.00
0.05
0.10
0.15
0.20
0.25
0.30
0.35
0
20
40
60
80
100
X^B_Al (at.-%)

Figure 12

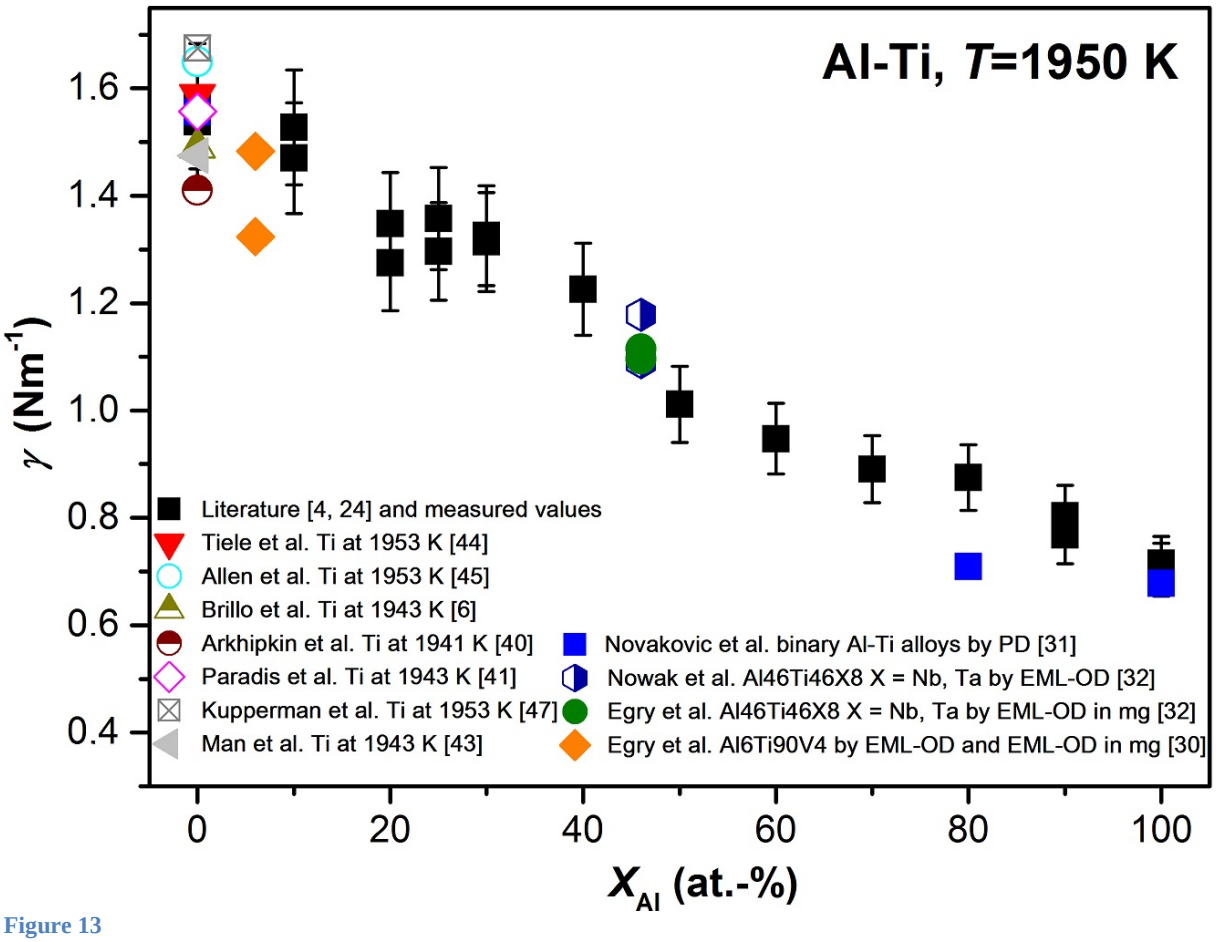
Al-Ti, T=1950 K
γ (Nm-1)
1.6
1.4
1.2
1.0
0.8
0.6
0.4
0
20
40
60
80
100
XAl (at.-%)
Literature [4, 24] and measured values
Tiele et al. Ti at 1953 K [44]
Allen et al. Ti at 1953 K [45]
Brillo et al. Ti at 1943 K [6]
Arkhipkin et al. Ti at 1941 K [40]
Paradis et al. Ti at 1943 K [41]
Kupperman et al. Ti at 1953 K [47]
Man et al. Ti at 1943 K [43]
Novakovic et al. binary Al-Ti alloys by PD [31]
Nowak et al. Al46Ti46X8 X = Nb, Ta by EML-OD [32]
Egry et al. Al46Ti46X8 X = Nb, Ta by EML-OD in mg [32]
Egry et al. Al6Ti90V4 by EML-OD and EML-OD in mg [30]

Figure 13